Author Contributions:

Conceptualization: Ke Che
Data curation: Thomas Lauvaux, Noemie Taquet, Wolfgang Stremme, Carlos Alberti, Morgan Lopez, Philippe Ciais, Michel Ramonet, Michel Grutter
Formal analysis: Ke Che
Funding acquisition: Michel Ramonet, Michel Grutter
Investigation: Ke Che
Methodology: Ke Che
Resources: Thomas Lauvaux, Noemie Taquet, Wolfgang Stremme, Philippe Ciais, Michel Ramonet, Michel Grutter

Urban XCO₂ Gradients From a Dense Network of Solar Absorption Spectrometers and OCO-3 Over Mexico City

Ke Che[1,2,3] ![ORCID], Thomas Lauvaux[2], Noemie Taquet[4], Wolfgang Stremme[4], Yang Xu[3] ![ORCID], Carlos Alberti[5] ![ORCID], Morgan Lopez[3] ![ORCID], Agustín García-Reynoso[4] ![ORCID], Philippe Ciais[3] ![ORCID], Yi Liu[1], Michel Ramonet[3] ![ORCID], and Michel Grutter[4] ![ORCID]

[1]Institute of Atmospheric Physics, Chinese Academy of Sciences, Beijing, China, [2]Groupe de Spectrométrie Moléculaire et Atmosphérique, University of Reims Champagne Ardenne, Reims, France, [3]Laboratoire des Sciences du Climat et de l'Environnement, IPSL, CEA-CNRS-UVSQ, Université Paris-Saclay, Gif sur Yvette Cedex, France, [4]Centro de Ciencias de la Atmósfera, Universidad Nacional Autónoma de México, Mexico City, Mexico, [5]Karlsruhe Institute of Technology, Institute of Meteorology and Climate Research, Karlsruhe, Germany

Abstract Satellite measurements of urban CO₂ plumes offer a global approach to track CO₂ emissions for large cities. To examine and to quantify the feasibility of space-based monitoring, an intensive measurement campaign (MERCI-CO₂) using seven solar-tracking Fourier transform infrared (FTIR) spectrometers has been conducted over the Mexico City Metropolitan Area (MCMA) to monitor urban emissions and to evaluate Snapshot Area Map (SAM) observations from the NASA's Orbiting Carbon Observatory-3 (OCO-3) mission. Once adjusted for their respective averaging kernels, we diagnosed a positive difference between OCO-3 and FTIR column measurements (1.06 ppm). Thanks to this unprecedented amount of column observations over a large city, we demonstrate that XCO₂ gradients within OCO-3 SAMs align with the inter-calibrated FTIR measurements (mean bias of 0.3 ppm), confirming the potential to track CO₂ emissions from space over large metropolitan areas. XCO₂ urban-rural differences across the FTIR network, show a strong correlation with observed gradients, with Pearson's correlation coefficients (R) around 0.92. The correlation is significantly lower when considering intra-urban gradients, where R drop to around 0.24. Simulated XCO₂ enhancements (ΔXCO₂) based on X-STILT for both FTIR and OCO-3 show relatively high correlations (R is around 0.6) using high-resolution footprints and two gridded inventories. Spatial correlations with OCO-3 improve when aggregating satellite retrievals at coarser resolutions (10 km). Our study demonstrates the capabilities of detecting urban gradients by FTIR network and OCO-3 SAM observations over MCMA, a promising result to evaluate the evolution of MCMA's emissions over the coming decade.

Plain Language Summary Despite the fact that large metropolitan areas across the world account for a significant fraction of the global CO₂ emissions from fossil fuels, city-scale CO₂ emissions estimates from inventories remain highly uncertain and usually lag real time by several years. Observations obtained from satellites and ground-based sensors are expected to improve the quantification of CO₂ emissions in urban regions. Observed CO₂ gradients (site-to-site differences) over urban areas is essential for quantifying CO₂ emissions. In this study, we assess intra-urban CO₂ gradients over the Mexico City Metropolitan Area utilizing dense observations from both space and ground. Our analysis reveals that space and ground observations exhibit greater consistency when comparing urban-to-rural gradients, as opposed to gradients observed exclusively within urban areas. Furthermore, simulated urban gradients based on inventories show good coherence with our observed gradients, underscoring the potential for utilizing both space and ground spatial gradients in city-scale CO₂ emissions estimation.

1. Introduction

Urban areas are home to billions of people, sources of about 70% of fossil-fuel CO₂ emissions at the global scale. Hence, metropolitan areas offer unique opportunities for carbon emission mitigation through local policies to combat climate change (Stocker, 2014). But decarbonization requires widely different strategies across cities (Linton et al., 2022). International consortiums (such as C40 City, Covenant of Mayors) have formed to provide guiding principles and to support mitigation plans for large metropolitan regions. Effective urban-scale mitigation strategies require a deep understanding of CO₂ emissions at city-scale (Hsu et al., 2020).

Both bottom-up and top-down approaches have been applied across multiple metropolitan areas to quantify urban-scale CO_2 emissions (Gately & Hutyra, 2017; Lauvaux et al., 2016, 2020). While bottom-up methods provide a mechanistic and sectoral understanding of anthropogenic emissions, large uncertainties (such as downscaling method, spatial-temporal proxies, self-reported data etc.) still affect current gridded bottom-up inventories at urban scale (Gately & Hutyra, 2017), most often leading to under-estimation of urban direct emissions (Gurney et al., 2021). Observed variations in atmospheric CO_2 are used to constrain urban CO_2 emissions in inversion frameworks (top-down method) and provide powerful support to emission verification (Lauvaux et al., 2020). To date, only few studies have examined the potential use of column-integrated data to constrain urban emissions. Vogel et al. (2019) used five portable FTIR sensors over Paris to identify that the local XCO_2 gradient in Paris is primarily influenced by fossil fuel CO_2 with a strong impact from biospheric CO_2 sink on diurnal CO_2 variations. Jones et al. (2021) used five portable FTIR sensors to estimate diffuse methane emissions over Indianapolis, revealing a significant underestimation by bottom-up inventories. Similarly, Ionov et al. (2021) assimilated XCO_2 retrievals from two mobile FTIR sensors to quantify the anthropogenic CO_2 emissions from St Petersburg, resulting in a 3-fold increase in whole-city emissions compared to the municipal inventory. Che et al. (2022) inverted anthropogenic CO_2 emissions from Beijing using urban-rural differential FTIR observations and narrowed the uncertainties across several inventories. Zhao et al. (2022) identified missing methane sources near Munich using a network of five FTIR sensors. Compared to near-surface in-situ ground-based measurements, column-integrated measurements represent a larger area and are less affected by vertical transport errors (Lauvaux & Davis, 2014; Wu et al., 2018).

Satellite missions like NASA's Orbiting Carbon Observatory-3 (OCO-3) can also provide column-averaged CO_2 measurements over a specific region in "Snapshot Area Map" (SAM) mode with shorter revisit time compared to the polar orbital carbon-observing satellites like GOSAT (Shim et al., 2019), OCO-2 (Rißmann et al., 2022; Ye et al., 2020) or TanSat (Yang et al., 2020, 2023). SAMs assembled with several swaths from OCO-3 can capture spatial gradients across CO_2 city plumes, enhancing the potential for source detection and quantification compared to single swaths from typical orbits (Kiel et al., 2021). Assimilating multiple SAMs can potentially reduce emissions uncertainties as demonstrated with synthetic data (Kuhlmann et al., 2020; Roten et al., 2022). However, satellite-borne sensors are sensitive to scattering effects by aerosols or by artifacts from different land coverages (Crisp et al., 2004). Hence, satellite observations require precise evaluation and validation using ground-based column observations (Yang et al., 2020; Yoshida et al., 2013) especially at the city scale to quantify spatial gradients across a complex landscape (Butz et al., 2022). The NDACC (Network for the Detection of Atmospheric Composition Change) (De Mazière et al., 2018), Total Carbon Column Observing Network (TCCON) (Wunch et al., 2011) and COCCON (Collaborative Carbon Column Observing Network) (Frey et al., 2019) are three international remote sensing Fourier Transform Infrared Spectrometer (FTIR) networks that provide ground-based column measurements to evaluate several satellite products. All TCCON sites use IFS-125HR or similar high resolution FTIR spectrometers (Bruker Optics GmbH), which uses the direct solar near-infrared absorption spectrum to retrieve the column concentrations of CO_2 with an accuracy of 0.25% or less than 1 ppm (Wunch et al., 2011). Because TCCON stations remain sparsely distributed, portable EM27/SUN spectrometers have been developed by the Karlsruhe Institute of Technology (KIT) in cooperation with Bruker Optics GmbH (Gisi et al., 2012; Hase et al., 2016) and can be an effective complement to cover various surface types and regions across the globe. The COCCON network has been established with these instruments in order to standardize the calibration procedures, measurements and spectral analysis and have been widely used in studies to derive urban emissions, like in Berlin (Hase et al., 2015; Zhao et al., 2019), Paris (Vogel et al., 2019), Munich (Dietrich et al., 2021; Rißmann et al., 2022; Zhao et al., 2022), Indianapolis (Jones et al., 2021), Beijing (Cai et al., 2021; Che et al., 2022), and St Petersburg (Ionov et al., 2021).

The separation of anthropogenic urban signals from the highly-variable background inflow remains challenging (Schuh et al., 2021). Strategic deployment of FTIR stations have usually been involved both in upwind-rural and polluted city deployments in order to extract the urban signals (Chen et al., 2016; Shekhar et al., 2020). However, dominant winds often overlap with fossil fuel sources from other regions (Hu et al., 2018; Wei et al., 2020). Boundary inflow concentrations can also be determined from global coarse-resolution models combined with finer-grid simulations to determine the background values (Monteil & Scholze, 2021; Rastogi et al., 2021; Schuh et al., 2021). Sargent et al. (2018) filtered Carbon-Tracker background values by comparing modeled concentrations to near-surface measurements to reduce the boundary inflow errors. Improving the background values

along with the city emissions within the inversion framework is also an effective way to obtain more robust results (Jones et al., 2021; Maasakkers et al., 2022).

The Mexico City Metropolitan Area (MCMA) contains around 21 million inhabitants, or about 20% of the entire population of Mexico. MCMA has become the most populous urban region in North America and the fourth largest megacity worldwide according to the United Nations's estimates in their 2022 revision of World Urbanization prospects. Pollutants from MCMA have been detected and measured by ground- and space-based column observations (Borsdorff et al., 2020; Stremme et al., 2013). According to the inventories, CO_2 emissions in MCMA represent around 9% of the national emissions of Mexico, dominated by transportation (Molina et al., 2019). Mexico City's government has pledged to reduce its greenhouse gas emissions by 30% by 2030 from their business-as-usual scenario and to achieve carbon neutrality by 2050. The MCMA has been selected as a frequent SAM target by OCO-3. In parallel, a dense network of seven ground-based column sensors located within MCMA has been deployed as part of the Mexico City's Regional Carbon Impacts (MERCI-CO_2) project in 2020–2021, offering a unique opportunity to evaluate XCO_2 gradients observed by the OCO-3 SAM's, and for the quantification of intra-city XCO_2 gradients.

In this study, we focus on the intra-city XCO_2 gradients over MCMA based on two column data sets: FTIRs and OCO-3. To validate the detection capability of OCO-3 over the MCMA, we present the comparison of XCO_2 and site-to-site XCO_2 differences from these two observing strategies. Then, we applied a Lagrangian particle dispersion model (WRF-XSTILT) to simulate XCO_2 urban enhancements based on two independent emission inventories (UNAM_EMI and ODIAC). We constructed vertical columns of CO_2 from a global inversion system as background. Finally, we compared the simulated and observed enhancements from FTIR and OCO-3 to evaluate the accuracy of our two inventories over MCMA.

2. Data Set and Methodology

2.1. MERCI-CO_2 FTIR Campaign

Seven solar-viewing Fourier transform infrared (FTIR) spectrometers were deployed during an intensive 7-month field campaign (part of the French-Mexican project MERCI-CO_2) in the MCMA area during October 2020 to May 2021 (Figure 1). One FTIR has been continuously operated since 2012 from an NDACC station (Altzomoni Atmospheric Observatory) located on a mountain top (3,985 m a.s.l), which is 60 km from Mexico City. This high-resolution IFS 120/5HR (spectral resolution <0.02 cm^{-1}) spectrometer performs regular NDACC and XCO_2 TCCON-like measurements using alternate optical components and retrieval strategies (Baylon et al., 2017) but producing similar results. Two low-resolution portable EM27/SUN (spectral resolution <0.5 cm^{-1}) (Gisi et al., 2012; Hase et al., 2016) FTIR instruments are permanently operated at the university campus (UNAM) South of the city, and at a northern site (Vallejo) since 2016 and 2019, respectively. The other 4 EM27/SUN instruments were deployed as part of the MERCI-CO_2 project and the results of this intensive field campaign are presented here.

FTIR observations were collected in cloudless daylight during 07:00-18:00 CDT (corresponding to 13:00-24:00 UTC). Each FTIR site was equipped with a weather station to measure the surface pressure and temperature. Non-linear least-squares fitting retrieval algorithms, PROFFASTv0 (03/2020) (Alberti et al., 2022) and PROFFITv9.6 (Hase et al., 2004) were used to process all EM27/SUN and IFS 120/5HR spectra, respectively, into the column-averaged carbon dioxide dry-air mole fraction (XCO_2). For the EM27/SUN, according to the COCCON procedure, the TCCON a priori profiles and meteorological data (GGG2014 version of MAP files) are used in the scaling retrievals (Tu et al., 2020). For the IFS 120/5HR, we used the WACCM (Whole Atmosphere Community Climate Model) a priori profiles, and followed the strategy described in Baylon et al. (2017). Several pre- and post-process quality filters were applied to discard data affected by clouds or volcanic ash, or with low signal, based on DC intensity signal, retrieval quality indicators (relative RMS, signal-to-noise ratio, wavenumber shift) and statistical criteria (standard errors). Noisy outliers were largely removed according to the 3-sigma criterion. All the EM27/SUN instruments are part of the COCCON network and have been calibrated at KIT next to the TCCON-KIT site and their measurements are traceable back to the World Meteorological Organization standards (Messerschmidt et al., 2011). Additionally, the six EM27/SUN were recalibrated once again in Mexico performing side-by-side measurements at the UNAM site for a duration of several days before and after the intensive campaign and it is introduced in detail in Taquet et al. (2024). Using as reference the EM27/SUN located at the UNAM (for which the longer time series was recorded since 2016), the KIT calibration coefficients were refined
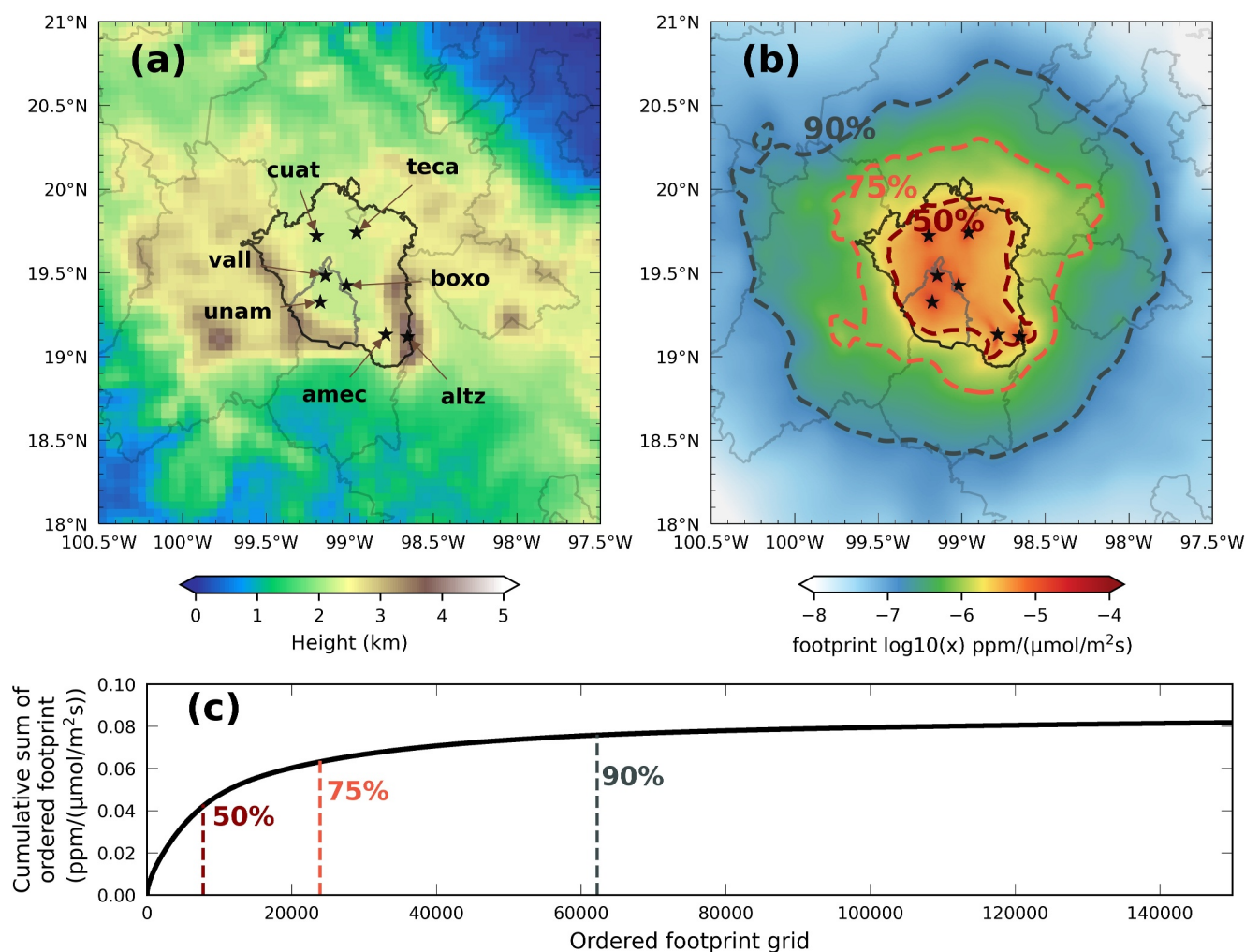
Figure 1. (a) The topography map for Mexico City Metropolitan Area (MCMA). Seven FTIR sites used in this study are marked with black stars. The outlier of MCMA is indicated with a black closed line and CDMX with gray; (b) Overall footprints for averaged footprint of all sites during study period with footprint contours of its 50, 75, 90 percentile level. The footprints depicted are based on the column footprints from X-STILT; (c) Cumulative sum of ordered footprints (high to low). 50%, 75% and 90% of the footprint sum values are indicated with dark red, orange, and dark blue dotted line.

by the inter-comparison. The high resolution (IFS 120/5HR) measurements were also calibrated using the same EM27/SUN reference instrument.

Detailed geographic information and measurement periods for each FTIR site are shown in Table 1. MCMA is in a valley surrounded by high mountains (Figure 1a), trapping polluted air parcels in the basin (Figure 1b). Two FTIRs were deployed in rural areas, one near the basin (AMEC) and the other on a mountain top (ALTZ), with significantly lower CO_2 emissions (<1 $\mu mol/m^2 s$) to observe background air masses around Mexico. Five instruments were located across the urban basin of Mexico City: three of them (UNAM, VALL and BOXO sites) in the core urban area (CO_2 emissions >10 $\mu mol/m^2 s$); the other two (CUAT and TECA sites) in peri-urban areas to characterize the full extent of the MCMA. Additionally, one EM27/SUN was temporarily deployed at the ALTZ site for the side-by-side inter-calibration and to circumvent an interruption in the IFS 120/5HR measurements between November 2020 and February 2021 due to the need of the laser replacement.

2.2. OCO-3 Observations

OCO-3 was launched in May 2019 and provides continuous online products since August 2019. Compared to OCO-2, OCO-3 added an agile 2-D pointing technique to capture XCO_2 80 × 80 km^2 SAMs with ~1.29 × 2.25 km^2 spatial resolution (Taylor et al., 2020). Thanks to its SAM mode, OCO-3 provides an

Table 1
The Information About the Position and Observation Period for Seven FTIR Sites Located Over Mexico City

Site name	Location	Instrument	Observation period	Class	CO_2 flux ($\mu mol/m^2 s$) UNAM_EMI	ODIAC
CUAT	19.72°N, 99.20°W 2.26 km	EM27/SUN	2020.10–2021.5	Inflow	6.24	6.05
TECA	19.74°N, 98.96°W 2.28 km	EM27/SUN	2020.10–2021.5	Inflow	1.32	2.07
UNAM	19.33°N, 99.18°W 2.28 km	EM27/SUN	Since 2016.3	Urban	14.93	10.47
VALL	19.48°N, 99.15°W 2.26 km	EM27/SUN	Since 2019.9	Urban	23.72	13.49
BOXO	19.42°N, 99.02°W 2.21 km	EM27/SUN	2021.2–2021.5	Urban	13.47	10.47
AMEC	19.13°N, 98.79°W 2.45 km	EM27/SUN	2020.10–2021.5	Background	0.25	0.64
ALTZ	19.12°N, 98.66°W 3.99 km	EM27/SUN IFS125 HR	2020.10–2021.2 Since 2012.5	Background	0.03	0.09

Note. It specifies each site's geographical coordinates (latitude and longitude) and altitude above sea level (a.s.l.). CO_2 fluxes within a surrounding circle with a 10 km radius for each site is also shown. Class column categorizes each site based on the CO_2 emissions in its vicinity.

unprecedented coverage of XCO_2 fine-scale spatial maps and more frequent revisit time to study sub-city scale CO_2 emissions performances (Kiel et al., 2021). MCMA has been selected for frequent scanning by OCO-3. Here, we used OCO-3 Level 2 bias-corrected XCO_2 data (version 10.4r) generated by the Atmospheric CO_2 Observations from Space (ACOS) algorithm (O'dell et al., 2018; Osterman et al., 2020). Inferior quality data are filtered based on the quality flag in the data set (xco$_2$_quality_flag = 0).

Ground-based FTIR observations are less affected by the heterogeneous surface properties or by scattering effects caused by cirrus and/or aerosols. Consequently, the accuracy of ground-based observations is usually higher than satellite observations (Wunch et al., 2011). Different colocation methodologies have been developed to compare FTIR and OCO-3 retrievals. Most approaches use averages of satellite retrievals within a predefined area (circle or square) centered on the ground-based site location. Similarly, an averaged FTIR value is computed within a specific time window, around the satellite overpass time. Nguyen et al. (2014) used a modified distance to calculate a weighted average of collocated data. Belikov et al. (2017) proposed a footprint-based method only selecting the satellite measurements influenced by the ground-based site to determine if the same air mass affected both column measurements. Over the intensive observation period, 34 co-located OCO-3 SAMs were collected with 20, 980 screened soundings (44.02% of the total satellite points). We only picked 20 high-quality overpasses with sufficient data density over MCMA. For OCO-3 XCO_2 validation, we selected and averaged FTIR data within 30 min of OCO-3 overpass times. OCO-3 data were averaged within a 10 km radius of each FTIR site. Each comparison requires at least 20 OCO-3 and 5 FTIR soundings to reduce the measurement errors.

After selecting matched data, we apply an averaging kernel correction following Rodgers and Connor (2003) and substitute the satellite a priori profile into the each FTIR retrieval before comparing FTIR data to OCO-3 data, as expressed by Equations 1–2:

$$X_{FTIR}^{adj} = X_{FTIR} + \sum_{i=1} PWK_i(AK - I)(x_{a,FTIR} - x_{a,OCO-3}) \tag{1}$$

$$PWK_i = \frac{\Delta P_i}{P_{surf}} \tag{2}$$

where X_{FTIR}^{adj} represents the FTIR retrieved total column using the satellite's a priori profile, while X_{FTIR} denotes the original FTIR retrieval, AK is the FTIR column averaging kernel, I is the unit vector, $x_{a,FTIR}$ and $x_{a,OCO-3}$ correspond to the a priori partial column profiles of FTIR and OCO-3 retrievals, respectively. PWK_i is the pressure weighing function of layer i, it weight the pressure thicknesses of each level (ΔP) relative to the surface pressure (P_{surf}) and used to integrate profile into column. Subsequently, X_{FTIR}^{adj} is employed for the comparison with X_{OCO-3}. Based on the matching criteria introduced previously, we found 47 to 50 FTIR observations within ±30 min of each OCO-3 overpass. Within a 10 km radius of an FTIR site, the number of OCO-3 observations
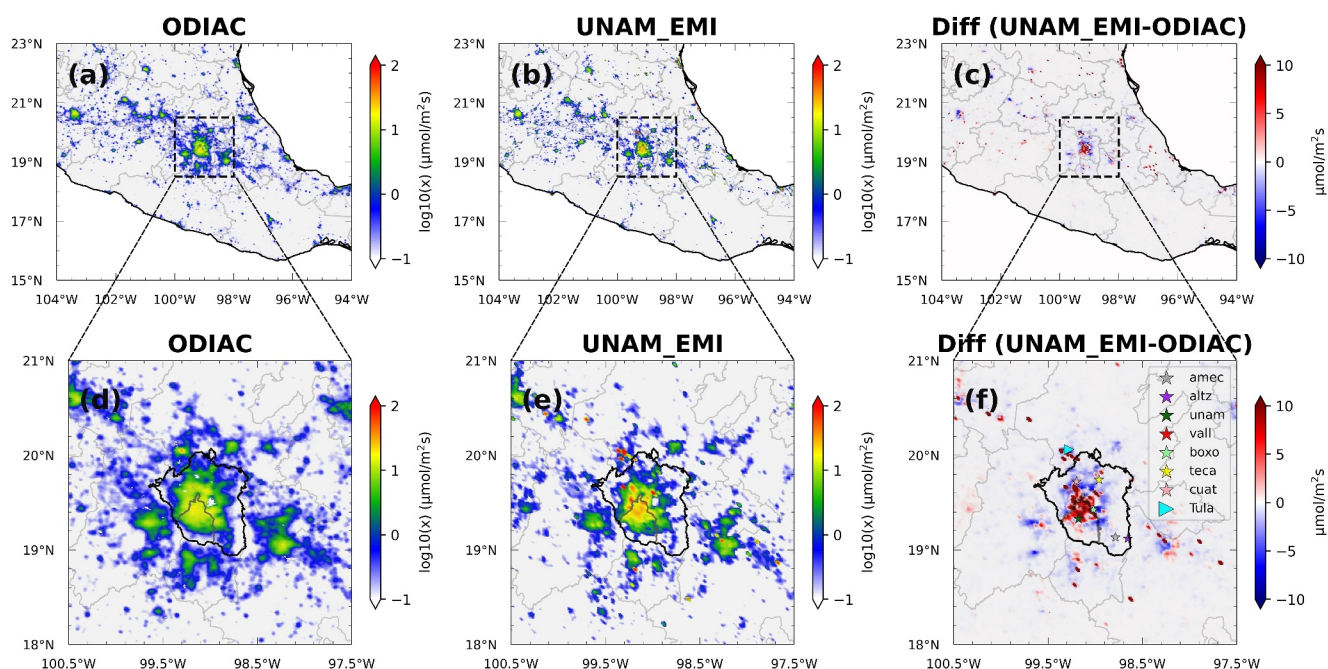
Figure 2. Map of CO_2 emissions (log10 (μmol/m^{2}s) from ODIAC (a, d) and UNAM_EMI (b, e) over Mexico (top row) and Mexico City Metropolitan Area (MCMA) (bottom row). (c, f) Differences between UNAM_EMI and ODIAC in CO_2 emissions (μmol/m^{2}s). The region denoted by CDMX corresponds to the political boundary of Mexico City (enclosed with a gray line). MCMA is indicated with black line.

ranged from 37 to 111. The a priori profiles for OCO-3 exhibit spatial variability, changing with latitude and across different pixels, while the a priori used for FTIR observations at each site is consistent, employing the same profile for all measurements within a single day. We applied the matched OCO-3 a priori profiles to all selected FTIR soundings, then averaged these values to obtain the X_{FTIR}^{adj} averages, and compared them with the averaged original OCO-3 data. This method was employed to reduce the impact of different a priori profiles between the data sets.

2.3. Modeling System

2.3.1. Emission Inventories and Biogenic Fluxes

Two fossil fuel emissions products were used as a priori emissions: the Open-source Data Inventory for Atmospheric Carbon dioxide (ODIAC) version 2020 (Oda & Maksyutov, 2015), and a national bottom-up inventory developed by the Environmental Ministry and converted for model use by National Autonomous University of Mexico (UNAM_EMI). ODIACv2020 provides monthly gridded emissions at 1 km × 1 km spatial resolution for the year 2019, it is worth noting that the ODIAC version 2020 data set is not the most current version available now, however, it was the latest data set at the onset of our study (Oda & Maksyutov, 2015). The Temporal Improvements for Modeling Emissions by Scaling (TIMES) product offers global weekly and diurnal scaling factors (Nassar et al., 2013). These factors are applied to downscale monthly ODIAC estimates, converting them into hourly estimates. UNAM_EMI, anchored in the 2016 Mexico National Inventory, yields hourly anthropogenic CO_2 emissions estimates and is instrumental for air quality management in Mexico City. Developed with support from the Environmental Secretariat of Mexico City (SEDEMA, 2018), its validity and precision have been corroborated through evaluations by Rodríguez Zas and Garcia-Reynoso (2021), along with Pacheco et al. (2020). CO_2 emissions have been organized into three main sectors: area sources (residential/commercial), mobile sources (traffic), and point sources (industrial). The data underpinning these spatial and temporal profiles are openly accessible via UNAM_EMI model created by the National Autonomous University of Mexico (UNAM) (García-Reynoso et al., 2018). The procedure for converting from annual to hourly can be found in García-Reynoso et al. (2018). Leveraging this model, we have meticulously generated 3 km hourly $CO_{2_{ff}}$ (fossil fuel CO_2) emissions profiles. UNAM_EMI CO_2 emissions calculated with a spatial resolution of 3 km over central Mexico were then regrided at 1 km resolution using a flux conservative method. Fossil fuel CO_2 emissions

from both inventories are affected by the Tula power plant using oil and gas (Sosa et al., 2020) (Figures 2a–2c). The two inventories show significant differences in the intra-urban region (Figures 2d–2f): the total UNAM_EMI emissions are 33.3% higher than ODIAC over the MCMA (black enclosed line) and 44.4% higher over Mexico City (Ciudad de México, CDMX, gray enclosed line). Spatially, the UNAM_EMI shows higher values than ODIAC (37.0%) in the most central part of MCMA, while ODIAC emissions extend further away from the city center (Figure 2f). Because ODIAC downscales national-level emission statistics from the Carbon Dioxide Information Analysis Center using nighttime light data from the Defense Meteorological Satellite Program satellite, sources are usually more diffuse, increasing differences at the urban-rural transitioning areas (Oda et al., 2018). The correlation between night light intensity and CO_2 emissions also tends to be not significant from dense urban areas, especially for developing countries (Chen et al., 2020). CO_2 emissions from energy production are based on worldwide large point emission sources (power plants/companies) from Carbon Monitoring for Action database (CARMA), corrected for misattribution (Oda et al., 2018).

For the biogenic fluxes, we used the Net Ecosystem Exchange (NEE) data sets simulated by the Carnegie-Ames-Stanford Approach (CASA) biosphere model (Feng et al., 2021; Y. Zhou et al., 2020). The CASA model version, based on a light-use efficiency parameterization and including historical forest disturbance data, was run in ensemble mode using various perturbed parameters to represent the uncertainties in NEE fluxes. The simulations cover North America and Central America at high spatial and temporal resolutions (5-km, 3-hr) over Mexico. As previously used in atmospheric studies (Feng et al., 2021), we coupled the parameter-based ensemble member corresponding to intermediate values for both maximum photosynthesis (E_{max}) and respiration (Q10), producing the best performances over North America (Y. Zhou et al., 2020).

2.3.2. Atmospheric Modeling System

The influence functions of column-averaged measurements were computed using the column version of the Stochastic Time-Inverted Lagrangian Transport model (X-STILT based on Hysplit v5.1) (Wu et al., 2018) to establish a source-receptor sensitivity link of the column measurements to the upstream emissions. X-STILT was driven by hourly meteorological fields simulated by the Weather Research and Forecasting (WRF) model (version 3.9.1.1). In our case, the WRF model configuration includes three horizontal grid spacing ranging from 15 km for the outermost domain, telescoping to 3 km in the middle domain and 1 km for the innermost grid (encompassing the whole MCMA region). ECMWF Reanalysis v5 (ERA5) data set were used as the initial and boundary conditions (Hersbach et al., 2022). 50 vertical levels are used from the surface to 50 hPa. Mellor-Yamada Nakanishi and Niino Level 2.5 (MYNN) was selected for the PBL physics option and the single-layer urban canopy model was chosen to represent the urban surface interactions. The performance of this configuration was evaluated in (Xu, 2023) and Deng et al. (2017). WRF model performances were evaluated using meteorological surface stations across the MCMA region, both for wind speed and direction, in addition to the PBL height evaluation using a Lidar instrument deployed at the UNMA site to the South of MCMA. During the afternoon time period, the mean errors vary from −580 m (in January) to 110 m (in May) for the PBL height. Considering wind speed near the surface, the mean error and mean absolute errors vary from −0.36 to −0.72 m/s and from 1.28 to 2.00 m/s, respectively. These model performances remain equivalent to other previous modeling studies in mountainous metropolitan areas such as Feng et al. (2016) over the basin of Los Angeles, or Pérez-Landa et al. (2007) over Valencia, Spain.

X_{foot} from X-STILT model represents the sensitivity of the column measurements to the surrounding surface-atmosphere fluxes. For each receptor (r), X_{foot} with units of ppm/μmol/m^{2}s is calculated as follows:

$$X_{foot}(x_r, t_r | x_k, y_k, t_m) = \frac{m_{air}}{h\overline{\rho}(x_k, y_k, t_m)} \frac{1}{N} \sum_{k=1}^{N} \Delta t_k(x_k, y_k, t_m) AK(r) PWK(r) \tag{3}$$

where (x_r, t_r) is the receptor (r) location, (x_k, y_k, t_m) is the model's initial time set, denoted by the model grid coordinates that encompass both location and time, is the mean molar mass of dry air (defined as 29 g mol^{-1}), h is the atmospheric column height, $\overline{\rho}$ is the mean density of the air below h, N is the total number of released particles, Δt_k is the residence time of particle k spent in the grid cell (x_k, y_k, t_m). The total column footprint (X_{foot}) is obtained by integrating the footprints from different altitudes, convolved with a pressure weighting function $PWK(r)$ and an averaging kernel $AK(r)$ at the receptor location.

The locations of receptors correspond to the seven FTIR sites and to all the available OCO-3 XCO_2 retrievals measurements. For each receptor, an ensemble of 5,500 particles evenly distributed between 0 and 5,500 m (a.g.l) altitudes were traced backward in time for 24 hr. For the release of the particle at each altitude, the latitude and longitude coordinate was adjusted to follow the path dictated by the solar zenith angle (SZA) and solar azimuth angle at each observation time. As defined by our cumulative statistics in Figure 1c, most particles can be traced around 85 km outside of MCMA. 5,500 m was set as our maximum released altitude. We determined that less than 0.1% of the particles released near the surface could reach 5,500 m altitude based on the backward tracking simulation. Turbulent motions within the PBL for urban sites remain below 2,000 m. PBL depth for mountain sites is below 500 m. Only convective systems are able to transport air masses above the PBL. Because FTIR instruments are operated only during clear-sky conditions, the probability of encountering strong convective events remains low. The backward trajectory duration is determined through a sensitivity analysis that spanned the entire observation period, utilizing settings extending 48 hr into the past. By integrating the column footprints (generated by X-STILT) with emissions data (UNAM_EMI for anthropogenic sources and CASA for biogenic sources), we noted that the enhancements in XCO_2 are significantly diminished with a 24-hr backward setting (Figure S1 in Supporting Information S1), indicating that adopting a 24-hr period as an optimal backward setting for our analysis.

2.4. Local Influence and Background Concentrations

The X-STILT model simulates particles backward-in-time from the measurement locations to their final geographic locations (24 hr before). While the surface influence is defined by particles traveling near the surface, their final locations are used to generate the background concentration (initial conditions) of each column measurement. We describe here the simulation of local enhancements and the calculation of the background concentrations. Footprints from X-STILT (X_{foot}) are convolved with emission inventories to simulate the XCO_2 enhancements ($\Delta XCO_{2,sim}$) over each receptor (Equation 4). Anthropogenic emissions (E_{anthro}) are from ODIAC and UNAM_EMI, while the biogenic contribution (E_{bio}) is from the CASA biosphere model.

$$\begin{aligned} \Delta XCO_{2,sim} &= \Delta XCO_{2,anthro} + \Delta XCO_{2,bio} \\ &= X_{foot} \times E_{anthro} + X_{foot} \times E_{bio} \end{aligned} \quad (4)$$

The Observed XCO_2 enhancements ($\Delta XCO_{2,obs}$) are computed by using XCO_2 measurements obtained from both urban and background sites:

$$\Delta XCO_{2,obs} = XCO_{2,obs} - XCO_{2,back} \quad (5)$$

However, observed background values are not always accessible and relying exclusively on background site data for background values results in under-utilization of data. To address this, we used modeled boundary values from the Copernicus Atmosphere Monitoring Service (CAMS) data set as substitutes. According to Equation 6, Our simulated backgrounds ($XCO_{2,back,\ CAMS}$) comprises the weighted slant columns extracted from CAMS (global inversion-optimized greenhouse gas fluxes and concentrations, version: v21r2) and contribution from a priori profiles. The trajectory endpoints were extracted from the 4-D CO_2 mole fraction fields of the CAMS OCO-2 inversion product with a horizontal resolution of $1.9° \times 3.75°$ and a temporal resolution of 3 hr (Chevallier et al., 2019). Concentrations at higher altitudes (>5,500 m a.g.l) are complemented by the CAMS CO_2 profiles (x_{CAMS}) at the receptor locations. AK, a prior profile from FTIR and OCO-3 (x_a) and PWK are used to integrate vertical layers into column (Equation 6).

$$XCO_{2,back,CAMS} = PWK(AK x_{CAMS} + (I - AK) x_a) \quad (6)$$

$$XCO_{2,back,obs} = XCO_{2,back,CAMS} + \Delta XCO_{2,antrho} + \Delta XCO_{2,bio} \quad (7)$$

Background values from CAMS introduce uncertainty. Observed XCO_2 background values ($XCO_{2,back,obs}$) comprise three components: background XCO_2 ($XCO_{2,back,\ CAMS}$), fossil fuel-related ΔXCO_2 enhancements along the particles backward path ($\Delta XCO_{2,anthro}$), and biogenic ΔXCO_2 enhancements along the particles backward path ($\Delta XCO_{2,bio}$), as represented by Equation 7. To address this, we utilize the observed values
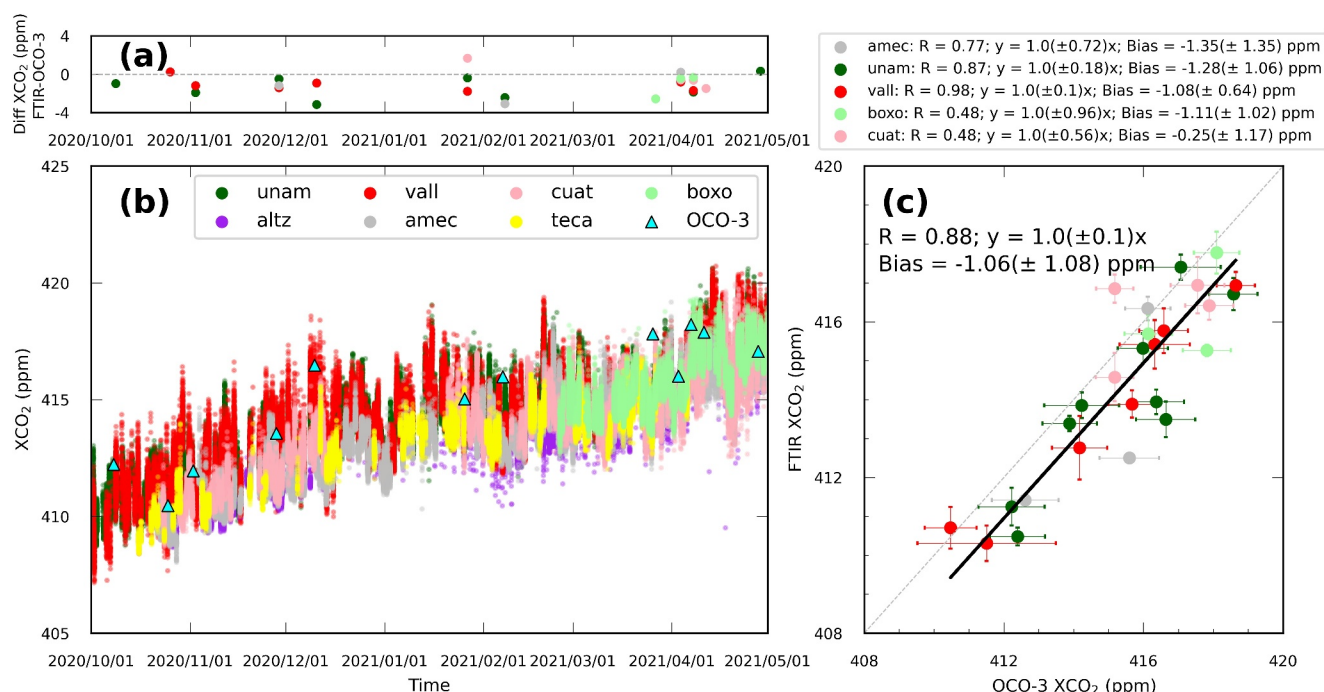
Figure 3. Difference (a), time series (b), and correlation plots (c) of XCO_2 from seven sites and co-located OCO-3 measurements. R represents the Pearson correlation coefficient. The thick black line represents the linear regression curve that is forced to pass through the origin point. Bias represents the mean and one standard deviation of the differences between y and x-axis. The error bars represent the uncertainty in the FTIR and OCO-3 measurements.

unaffected by anthropogenic and biogenic emissions for correction purposes. The selection criteria is to choose data points where absolute values of $\Delta XCO_{2,anthro}$ (from UNAM_EMI and ODIAC), $\Delta XCO_{2,bio}$ are all less than 0.1 ppm and the $\Delta XCO_{2,sim}$ is also less than 0.1 ppm. When ΔXCO_2 is close to zero, the observed $XCO_{2,back,obs}$ can be directly compared with $XCO_{2,back, CAMS}$ from CAMS. This correction method may introduce bias if certain emission sources or sinks are not adequately considered in the inventories. However, requiring several conditions to meet the specified requirements should help in reducing this uncertainty.

3. Results

3.1. Validation of XCO_2 From OCO-3 Using FTIR Measurements

The seven FTIR instruments were deployed at urban and rural sites across the MCMA based on the known anthropogenic inventory (UNAM_EMI, ODIAC) to collect column-averaged concentrations of CO_2. Measured XCO_2 for each site shows large variations at monthly (3.9–7.1 ppm) and daily (1.2–3.4 ppm) timescales. Column footprints were simulated by X-STILT to link the variations in concentrations observed in these sites with the different emission regions (Figure 1). These footprints are gridded at a 1 km resolution in both latitude and longitude. We arranged the footprint data in order and then performed a cumulative summation from highest to lowest values. Percentiles were determined as points at or below the fractional cutoffs (50%, 75%, 90%) of the summed ordered footprints. The impact of excluding points outside each contour region is clearly demonstrated by the steepness of the curve beyond each respective vertical cutoff (Figure 1c). Different percentile levels (50%, 75%, 90%) of the column footprints are outlined by dotted lines in both maps (Figure 1b) and for cumulative footprints (Figure 1c). The shape of the top-50% column footprint contour line overlaps with the topography contour lines, indicating that the particles stagnate in the basin with trapped air masses during the 24-hr backward simulations.

OCO-3 collects urban-focused XCO_2 measurements at high-resolution since its launch in 2019. A total of 20 partial XCO_2 maps are available over our intensive deployment period, with 16 of these maps being matched after applying the matching method introduced in Section 2.2. Figure 3b shows the observed XCO_2 retrievals as a function of time and Figure 3c shows the direct comparison of FTIR and OCO-3. The influence of different

averaging kernels and a priori profiles between ground-based and satellite measurements have been taken into account, as detailed introduced in Section 2.2. The difference between the original and the AK-adjusted FTIR data using satellite a priori profile is around 0.3 ppm. The average surface pressure used in OCO-3 (774.92 ± 7.17 hPa) is in agreement with the values used in FTIR (778.06 ± 6.79 hPa). Figure 3 (a, c) shows the comparison between FTIR observations from five stations and their co-located OCO-3 retrievals. We note here that TECA and ALTZ sites are not co-located with any OCO-3 retrievals. OCO-3 XCO_2 observations are highly-correlated with FTIR XCO_2 with a correlation coefficient (R) of 0.88 and a fitting slope near unity. OCO-3 XCO_2 values are however higher than FTIR values with a systematic bias of 1.06 ± 1.08 ppm and a Root Mean Square Error (RMSE) of 1.51 ppm. At most sites, FTIR XCO_2 measurements correlate with OCO-3 (R ranges from 0.77 ~0.98) except for BOXO and CUAT sites (R of 0.48). The mean systematic bias at each site varies from −1.35 to −0.25 ppm. AMEC shows the maximum bias (−1.35 ± 1.35 ppm), possibly due to the complex terrain in the vicinity of the station.

3.2. Comparison of the Urban-To-Rural XCO_2 Differences

XCO_2 differences between different sites ($\Delta XCO_{2,sts}$) are assumed to be representative of the local emissions. The AMEC and ALTZ sites, situated in rural regions with limited impact from human activities, serve as background sites for other sites. The other five sites located within the basin are heavily-influenced by anthropogenic emissions (seen from Table 1). The observed values at each urban site and their corresponding upwind values from background sites were separately analyzed under different wind conditions (see Figure S2 in Supporting Information S1). The time it takes for particles to travel from the background site to the urban site is determined by the footprint distribution at each backward time point. Our findings indicate that particles from urban sites typically reach the background sites within a maximum of 1 hour, with the majority (76.56%) arriving within 30 min (as shown in the insets in Figure S1 in Supporting Information S1). Over the 7-month period, the average XCO_2 values from VALL and UNAM were respectively 1.38 ± 1.16 ppm and 1.28 ± 0.84 ppm higher than the background values. In contrast, the XCO_2 values from BOXO, CUAT, and TECA, which are less influenced by anthropogenic emissions, showed only slight increases compared to the background sites (0.65 ± 0.77 ppm, 0.49 ± 1.04 ppm, and 0.36 ± 0.66 ppm, respectively). The XCO_2 differences between urban and background sites can be positive or negative, strongly dependent on the wind patterns (Figure S1 in Supporting Information S1). We categorize the wind direction as north and south, excluding the values with less significant north/south directions (comprising 23.41% of the total data). The main wind direction was north, representing 48.97% of the total, while the south direction accounted for 27.62%. Table S1 in Supporting Information S1 presents the relative frequencies of positive and negative urban-background differences for each urban site, specifically categorized under the wind directions of north and south. When the wind comes from the south, the AMEC/ALTZ sites serve as optimal background stations, and the observed enhancements at urban sites are predominantly attributed to the emissions within the MCMA. In this scenario, 92.63% of the urban-background XCO_2 gradients are positive. Conversely, with the wind coming from the north, the AMEC/ALTZ sites may be affected by urban emissions, resulting in a lower percentage of positive gradients (70.67%). The presence of negative gradients can be attributed to instances when northerly winds navigate paths that circumvent major urban emission sources. Consequently, these air-masses reach the rural sites (AMEC/ALTZ) without carrying urban contaminants. Furthermore, it is evident from Table S1 and Figure S2 in Supporting Information S1, that there are significant variations in the urban-to-rural differences and their positive percentages among different sites. Sites surrounded by high emissions, such as UNAM and VALL, consistently exhibit high positive gradient proportions around 90%, while the urban-to-rural differences remain consistent in different directions. On the other hand, TECA and CUAT show notable sensitivity to wind directions, with the positive percentage decreasing from 97.37% to 48.15% as we move from south to north, and a corresponding decrease in bias toward nearly zero.

The comparison of site-to-site differences from OCO-3 and FTIR observations is shown in Figure 4. There is no OCO-3 overpass over ALTZ, offering only AMEC as the main rural station for this comparison. The $\Delta XCO_{2,sts}$, representing the difference in XCO_2 between sites, exhibits variations within a maximum range of 3.03 ppm for FTIR and 1.56 ppm for OCO-3. The overall bias between the differences in pairs of sites for OCO-3 and FTIR is 0.3 ± 1.16 ppm, with R a equal to 0.45. OCO-3 is more compatible with FTIR ($R = 0.92$) when looking at the differences between urban and rural sites. But the intra-urban gradients show a lower correlation value ($R = 0.24$),
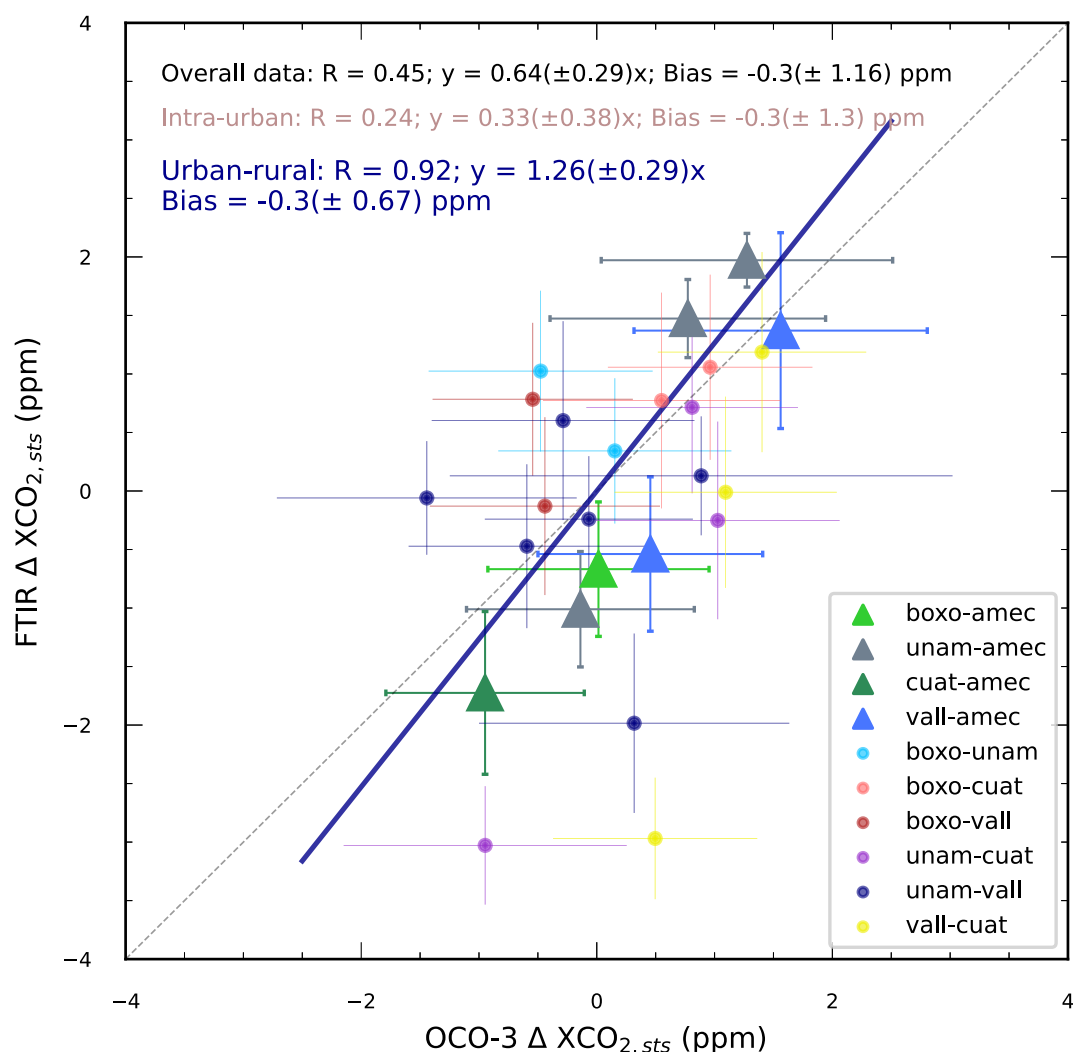
Figure 4. Scatter plots of site-to-site XCO$_2$ differences (ΔXCO$_{2,sts}$) between FTIR and OCO-3. The Error bars represent the uncertainty of ΔXCO$_{2,sts}$ observed by FTIR and OCO-3, accounting for uncertainties from both sites, and are calculated as detailed in $\sqrt{\sigma_{site1}^2 + \sigma_{site2}^2}$. The differences between urban and rural sites are shown in triangles. The difference between sites within the city is shown in circle points.

especially when considering the large degree of inhomogeneity around the urban sites with large enhancements caused by local fossil fuel emissions.

After using FTIR measurements to evaluate the OCO-3 intra-city gradients, we proceed to assess the simulated XCO$_2$ gradients corresponding to urban-to-background differences observed by FTIR. In this assessment, background values are obtained from observed values in either AMEC or ALTZ and exclude the incorporation of CAMS background values. As mentioned earlier (Section 3.2), the travel time between the background and urban sites is shorter than our time resolution (1 hr). Therefore, we utilized simultaneous observed data from both the urban and background sites for our analysis. Figure 5 presents the comparison results between the observed and simulated urban-to-background differences. Simulated ΔXCO$_{2,sts}$ results correlate with observations with an R value of 0.57 for UNAM_EMI and 0.53 for ODIAC. The slopes of the regression lines are 0.99 ppm ppm^{-1} for UNAM_EMI and 0.67 ppm ppm^{-1} for ODIAC. Histograms in Figure 5 (panels c–d) show the residuals, following a Gaussian distribution, with both biases around zero (0.48 ± 0.98 ppm for UNAM_EMI and −0.02 ± 0.94 ppm for ODIAC). Bias values suggest that the urban-to-rural gradients are slightly overestimated when considering the UNAM_EMI, but the higher values for R and near unity regression slope indicate the emission distribution seems more closely related to the actual emissions. We further analyze the impact of traveling time and observed that
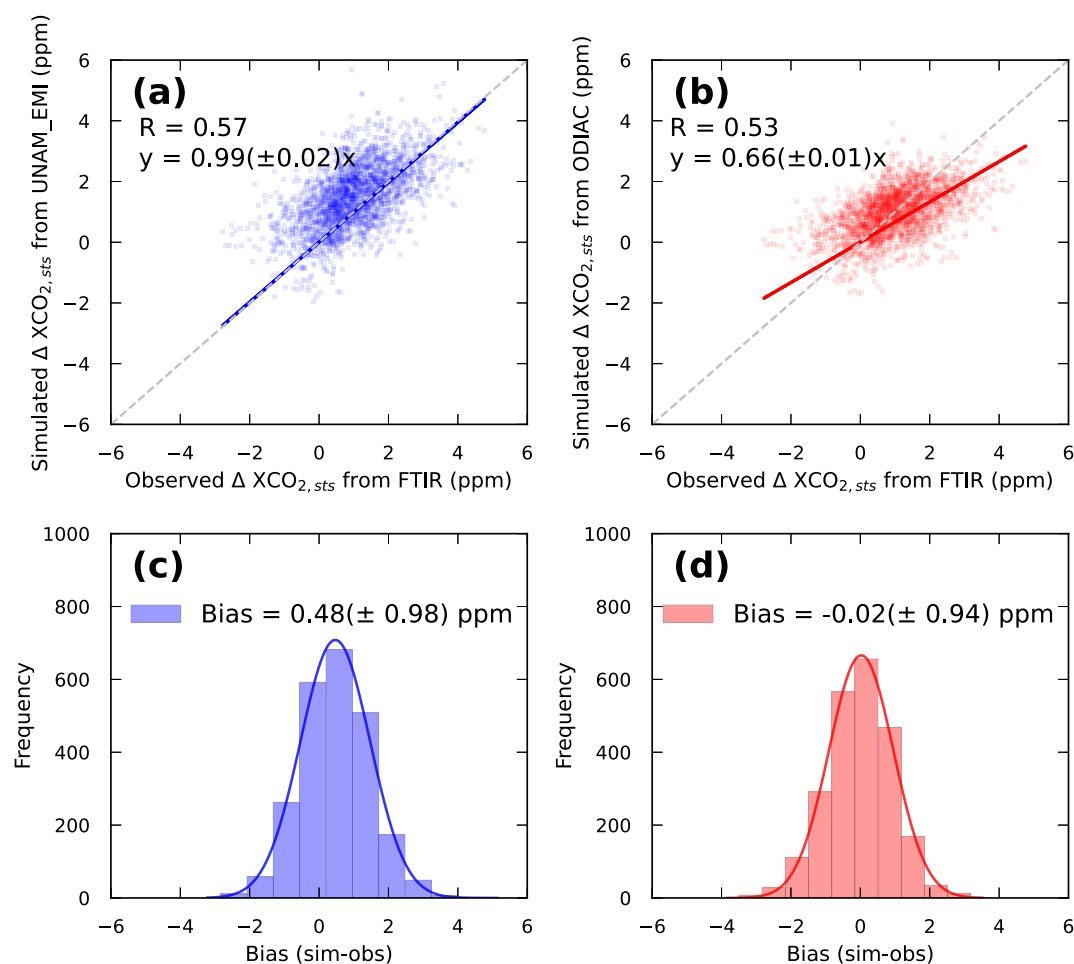
Figure 5. Upper panel: Scatter plots of observed and simulated urban to background site XCO_2 differences based on (a) UNAM_EMI and (b) ODIAC. Lower panel: Histograms of observed and simulated residuals for (c) UNAM_EMI and (d) ODIAC.

cases with traveling time exceeding 0.5 hr accounted for 23.44% of the total number of observations, while cases with traveling time less than 0.5 hr accounted for 76.56%. Our findings reveal that when the traveling time exceeds half an hour, the correlation decreases ($R = 0.48$ for UNAM_EMI, $R = 0.47$ for ODIAC), and the bias increases (0.65 ± 0.81 ppm for UNAM_EMI, 0.22 ± 0.75 ppm for ODIAC). However, when we only consider data points with a traveling time of less than 0.5 hr, the correlation increases ($R = 0.59$ for UNAM_EMI, $R = 0.54$ for ODIAC), and the bias decreases or remains nearly unchanged (0.43 ± 0.81 ppm for UNAM_EMI, -0.09 ± 0.75 ppm for ODIAC). These results suggest that shorter traveling time benefits the simulation of gradients between urban and background sites, as it leads to improved correlation and reduced bias.

When employing the differential approach (observed minus background) to derive urban gradients, it is notable that this method yields a low data utilization rate of 59.4% for urban FTIR sites, consequently leading to the under-utilization of background FTIR sites. OCO-3 data present limited coverage in the background region, with only three overpasses near the AMEC site, and exhibit significant variation in this region. This variability poses challenges in selecting suitable background values for each urban measurement.

3.3. Comparison of the Simulated and Observed Urban Enhancements

To enhance the utilization of observations, we now utilize the trajectory-endpoint CO_2 concentrations obtained from CAMS to determine the background concentrations (as described in Section 2.4). However, the uncertainty from the CAMS background should be taken into consideration. We also calculate the CAMS background for the observations which are barely affected by the anthropogenic or biogenic emissions and then compare to assess the
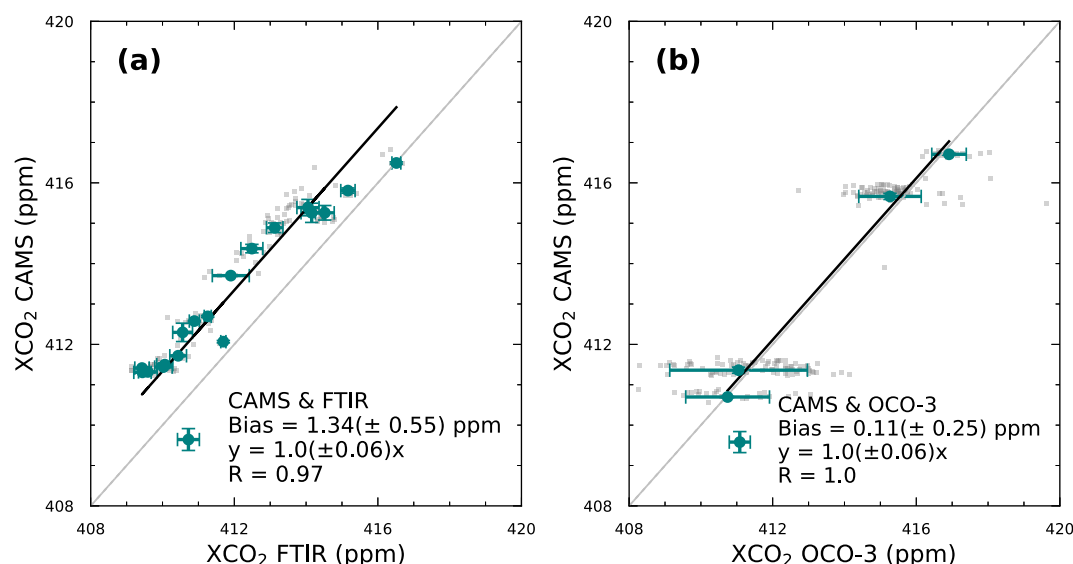
Figure 6. Scatter plots of observed XCO_2 values with minor anthropogenic or biogenic effects from (a) FTIR and (b) OCO-3 with the corresponding Copernicus Atmosphere Monitoring Service modeled background. Gray points represent the comparison for each observation. The green errorbar represents the daily mean and its one standard deviation.

error brought by the CAMS background. High correlations (R of 0.97 for FTIR, 1.0 for OCO-3) were found between the simulated and observed background XCO_2 values but with a systematic bias: 1.34 ± 0.55 ppm for FTIR and 0.11 ± 0.25 ppm for OCO-3 (Figure 6). We note that OCO-3 XCO_2 background values are more consistent with CAMS than FTIR. To determine if this lower bias of OCO-3 is a consequence of the OCO-2 assimilation in CAMS, we examined the CAMS product assimilating in-situ data (v21r1). However, the difference between CAMS-in situ and CAMS OCO-2 remains small (about 0.12 ppm). These biases from FTIR and OCO-3 exhibited an average difference of 1.22 ppm (1.337–0.115 ppm, with Figure 6 displaying only two significant numbers), which can be attributed to the inherent differences in observed values between the two instruments (1.35 ppm for AMEC background site, as depicted in Figure 3c). These biases were utilized to correct the CAMS background for both FTIR and OCO-3, respectively. This correction aimed to reduce the modeled background error and ensure consistent gradients across these two data sets. When comparing the observed ΔXCO_2 variations using CAMS as the background, we observe that the originally modeled CAMS background using AK and a priori from FTIR is consistently 0.39 (±0.11) ppm higher than OCO-3 (see Figure S3c in Supporting Information S1). We then applied corrections of −1.34 (±0.55) ppm and −0.11 (±0.25) ppm to CAMS in FTIR and OCO-3, respectively (see Figure 5). Consequently, the $XCO_{2,back,\ CAMS}$ in FTIR is 0.83 ppm lower than OCO-3. Considering that $XCO_{2,obs}$ in OCO-3 is, on average, 1.06 (±1.08) ppm higher than in FTIR (Figure 3c), we infer that the observed ΔXCO_2 (using CAMS as the background) in OCO-3 should be 0.23 ppm higher than in FTIR. This bias (0.23 ppm) aligns with the fact that the observed ΔXCO_2 (using observations as the background) in OCO-3 is 0.3 ppm higher than in FTIR (see Figure 4). Therefore, our correction aimed to reduce the modeled background error and ensure consistent gradients across these two data sets.

Figure 7 shows the comparison of simulated and observed urban enhancements after applying the corrective shift into the CAMS backgrounds. The simulated XCO_2 concentrations are highly-correlated with the observations (R of 0.9), with regression slopes approaching 1 for both UNAM_EMI and ODIAC emissions. The simulation also captures the spatial variability (R varied from 0.65 ~0.96) across the different sites. The contribution of urban enhancements resulting from anthropogenic and biogenic sources is relatively small compared to the CAMS background values, accounting for large fraction (99.7%) of the total XCO_2 values. As a result, different anthropogenic inventory (UNAM_EMI or ODIAC) would not be expected to significantly impact the XCO_2 comparison. The comparison to the observed urban enhancements (ΔXCO_2) using corrected CAMS values as background are shown in the second column of Figure 7. The correlation between simulated and observed ΔXCO_2 shows lower correlation values (R is 0.61 for UNAM_EMI and 0.57 for ODIAC). We note here that the
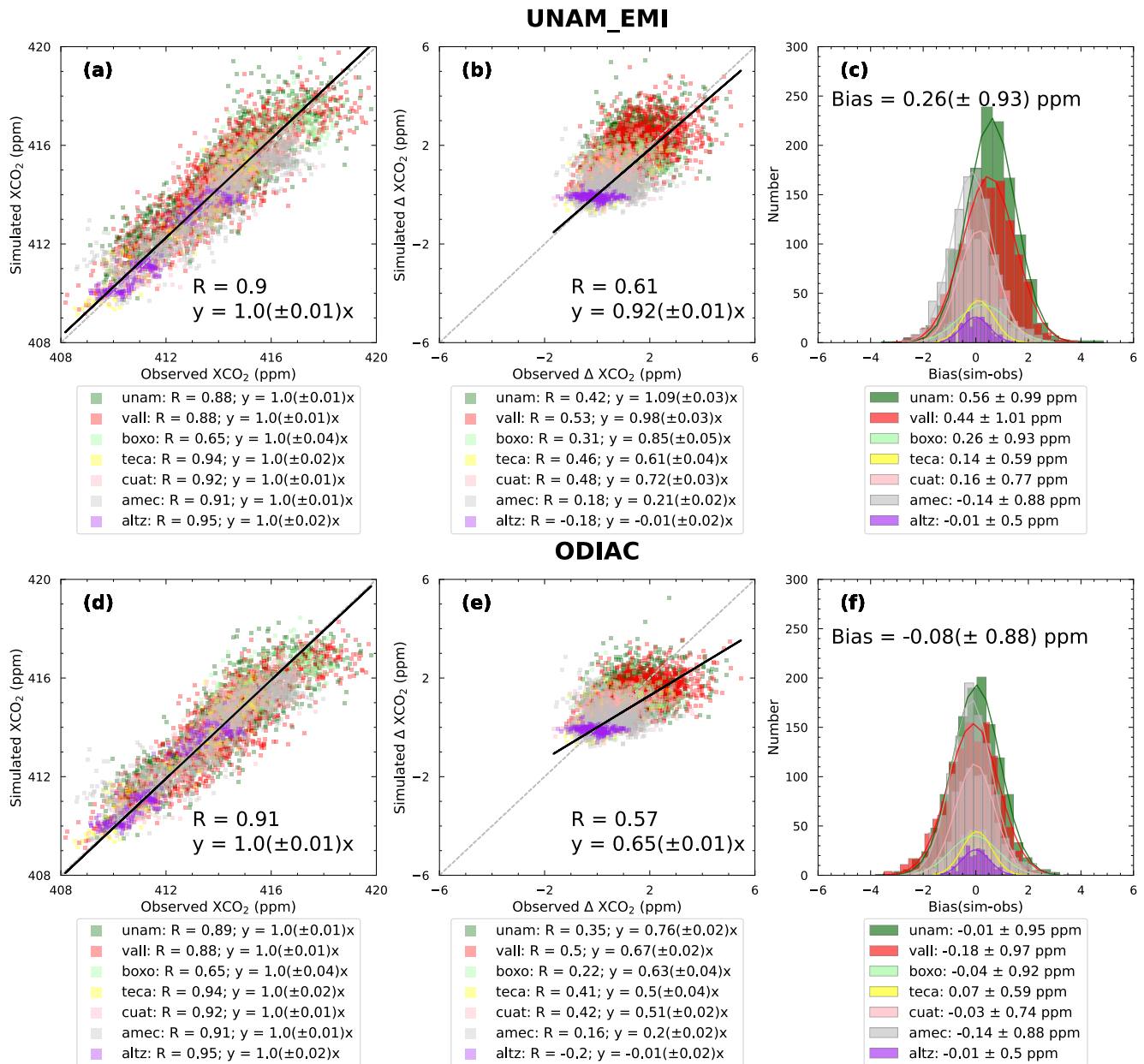
Figure 7. Comparison of the simulated and observed XCO_2 and XCO_2 enhancements (ΔXCO_2) at each FTIR site. The first row utilizes UNAM_EMI for anthropogenic emissions input in the simulation, while the second row uses the ODIAC inventory; both incorporate biogenic emissions data from CASA. The first column presents XCO_2 comparisons, the second column showcases ΔXCO_2 comparisons, and the third column displays histograms of the bias between simulated and observed values. Statistical values (R, fitting function, and bias) for each site are displayed beneath each subplot.

computed ΔXCO_2 values are a very small fraction of the total XCO_2 values (approximately 0.3% of XCO_2 values in magnitude), which could explain the lower statistical performances.

The range of simulated ΔXCO_2 and the relative contribution of the biogenic fluxes are shown in Table 2. For UNAM_EMI, the simulated ΔXCO_2 for each site ranges from: $-0.32 \sim 7.58$ ppm for UNAM; $-0.29 \sim 5.17$ ppm for VALL; $-0.54 \sim 3.79$ ppm BOXO; $-0.85 \sim 2.67$ ppm AMEC; $-0.68 \sim 3.85$ ppm for CUAT; $-0.72 \sim 1.94$ ppm for TECA; $-0.58 \sim 0.39$ ppm for ALTZ. For ODIAC, the simulated ΔXCO_2 value ranges vary from site to site: $-0.34 \sim 5.26$ ppm for UNAM; $-0.35 \sim 3.53$ ppm for VALL; $-0.78 \sim 2.84$ ppm for AMEC; $-0.47 \sim 3.04$ ppm for BOXO; $-0.64 \sim 2.25$ ppm for CUAT; $-0.70 \sim 1.93$ ppm for TECA; $-0.63 \sim 0.41$ ppm for ALTZ. The order of maximum simulated ΔXCO_2 differs in UNAM_EMI and ODIAC due to different distributions of statistical data.

Table 2
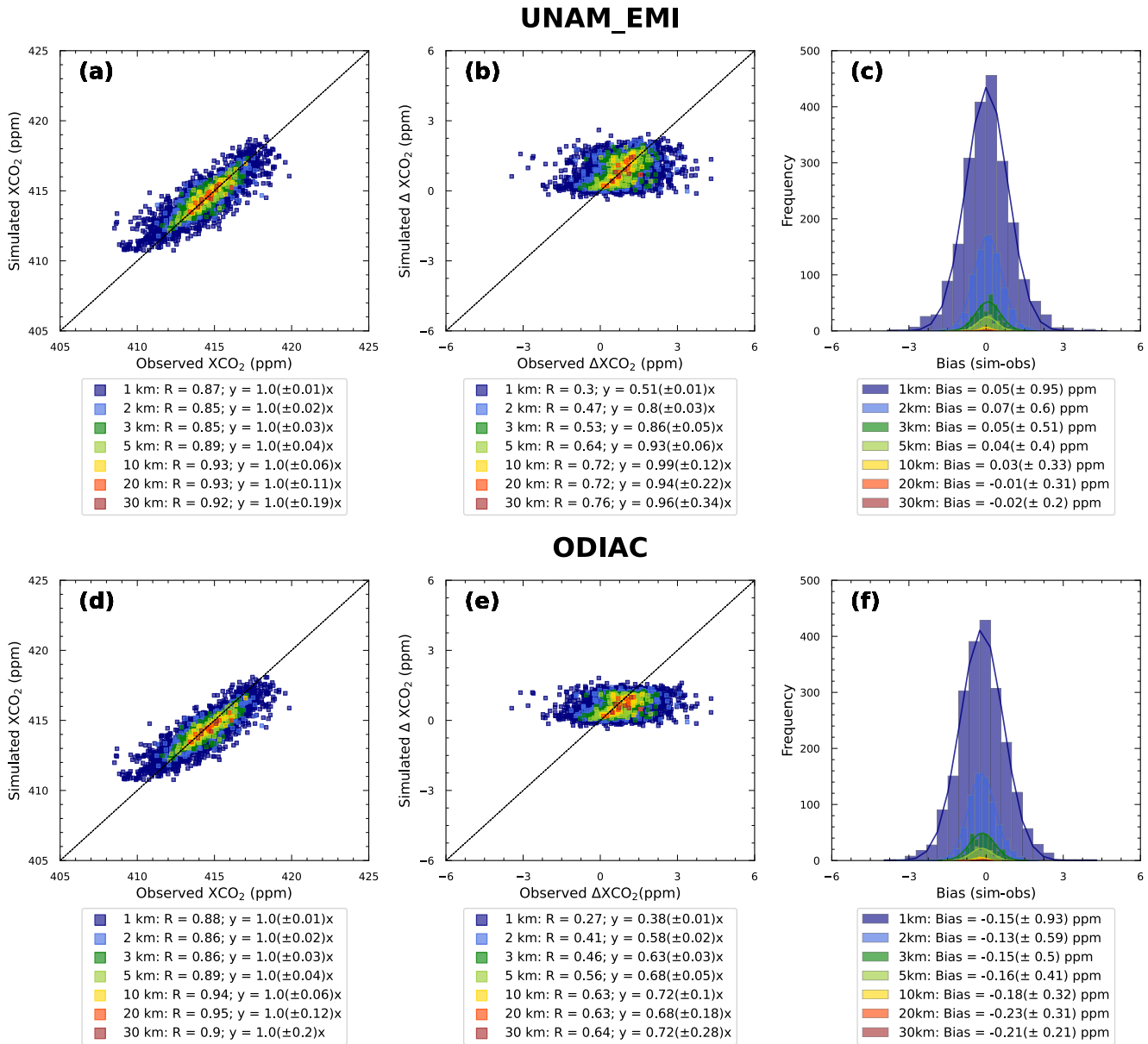*Simulated and Observed XCO$_2$ Enhancements (ΔXCO$_2$) for Each Site*

Site name	Simulated ΔXCO$_2$ UNAM_EMI + CASA *(Biogenic proportion)*	Simulated ΔXCO$_2$ ODIAC + CASA *(Biogenic proportion)*	Observed ΔXCO$_2$
CUAT	−0.68 ~3.85 ppm *(24.04%)*	−0.64 ~2.25 ppm *(25.95%)*	−1.66 ~3.64 ppm
TECA	−0.72 ~1.94 ppm *(33.16%)*	−0.70 ~1.93 ppm *(33.65%)*	−1.22 ~2.92 ppm
UNAM	−0.32 ~7.58 ppm *(10.01%)*	−0.34 ~5.26 ppm *(12.99%)*	−0.89 ~4.92 ppm
VALL	−0.29 ~5.17 ppm *(9.93%)*	−0.35 ~3.53 ppm *(13.00%)*	−1.17 ~5.47 ppm
BOXO	−0.54 ~3.79 ppm *(10.58%)*	−0.47 ~3.04 ppm *(12.06%)*	−0.89 ~3.34 ppm
AMEC	−0.85 ~2.67 ppm *(44.78%)*	−0.78 ~2.84 ppm *(43.04%)*	−1.58 ~3.29 ppm
ALTZ	−0.58 ~0.39 ppm *(78.33%)*	−0.63 ~0.41 ppm *(77.12%)*	−1.49 ~1.21 ppm

The influence of biogenic CO_2 emissions differs across sites: urban sites (UNAM, VALL, BOXO) with reduced biogenic signatures (biogenic only takes into account ~10%), inflow sites (CUAT, TECA) with intermediate influences (~28%) and background sites showing large biogenic contributions (especially for ALTZ site with 78% from biogenic fluxes). While AMEC was initially categorized as a background site due to its relatively low surrounding CO_2 emissions (Table 1), the wind direction over MCMA is mainly from the North over our study period, which brings more urban polluted air masses to the site. ALTZ is less susceptible to the local sources due to its high altitude, located further away from the basin.

Simulated and observed bias based on UNAM_EMI shows higher values (0.26 ± 0.93 ppm) compared to ODIAC (−0.08 ± 0.88 ppm), on average over the time period, especially for the higher CO_2 emissions in the center of the MCMA (Figure 2f). The regression slopes were 0.92 ppm ppm^{-1} for UNAM_EMI and 0.65 ppm ppm^{-1} for ODIAC. When focusing exclusively on the urban sites, the biases (0.38 ± 0.94 ppm for UNAM_EMI, −0.06 ± 0.9 ppm for ODIAC) and regression slopes (0.99 ppm ppm^{-1} for UNAM_EMI, 0.69 ppm ppm^{-1} for ODIAC) exhibit similarities to the results obtained from comparing urban-rural gradients without involving CAMS modeled background values. Specifically, the biases were found to be 0.48 ppm for UNAM_EMI and −0.02 ppm for ODIAC, while the regression slopes were 0.99 ppm ppm^{-1} for UNAM_EMI and 0.66 for ODIAC, as mentioned in the previous section. For the other urban sites, results from UNAM_EMI show correlation values from 0.31 ~0.53, and from 0.22 ~0.5 with ODIAC. For UNAM_EMI, the regression slope at urban sites is closest to 1 at UNAM (slope = 1.09 ppm ppm^{-1}), followed by VALL (slope = 0.98 ppm ppm^{-1}), BOXO (slope = 0.85 ppm ppm^{-1}), CUAT (slope = 0.72 ppm ppm^{-1}), and TECA (slope = 0.61 ppm ppm^{-1}). For ODIAC, the slope values ranked from high to low values is similar to slopes of UNAM_EMI: UNAM (slope = 0.76 ppm ppm^{-1}), VALL (slope = 0.67 ppm ppm^{-1}), BOXO (slope = 0.63 ppm ppm^{-1}), CUAT (slope = 0.51 ppm ppm^{-1}), and TECA (slope = 0.5 ppm ppm^{-1}). The mean errors and the standard deviations between simulated and observed XCO$_2$ values are 0.26 ± 0.93 ppm for UNAM_EMI and −0.08 ± 0.88 ppm for ODIAC. Compensating errors with UNAM_EMI emissions result in a combination of positive and negative biases across the different sites: UNAM and VALL show positive biases of 0.44 ~0.56 ppm; BOXO shows a slightly positive bias of 0.26 ppm; CUAT, TECA show 0.14 ~0.16 bias; AMEC and ALTZ show negative biases of −0.14 ~−0.01 ppm. As for ODIAC, biases are more consistent across our different sites with values varying from −0.18 to −0.07 ppm.

When directly comparing the OCO-3 XCO$_2$ values with the simulation, the correlation is about 0.9, with a regression slope near unity for UNAM_EMI and ODIAC (Figure 8). We evaluated the simulated ΔXCO$_2$ at high resolution (1 km), revealing a large random error around a mean value of 0.05 ± 0.95ppm with UNAM_EMI, and 0.15 ± 0.93 ppm with ODIAC. We then aggregated the simulated and observed OCO-3 values using coarser spatial resolutions (2, 3, 5, 10, 20 and 30 km) to evaluate the random errors (measurement noise or small scale transport errors). At coarser resolutions, the correlation significantly increased (R increased from 0.3 to 0.76 for UNAM_EMI, and from 0.27 to 0.64 for ODIAC) in ΔXCO$_2$. For the aggregation, we filtered out grid cells with few data points (less than 25% of the maximum number of points within one grid cell) to avoid partially-observed pixels. After aggregating OCO-3 data into 10- and 20-km grid cells, the regression slope tends to stabilize around unity for UNAM_EMI and 0.7 for ODIAC, which align with FTIR results. Mean differences between simulated and observed values are −0.02 ~0.07 ppm with UNAM_EMI and −0.21 ~-0.13 ppm with ODIAC.

The biases observed in the aggregated OCO-3 data (as shown in Figures 8c and 8f) are notably lower than those in the FTIR results (as shown in Figures 7c and 7f). Specifically, when applying a 10–30 km grid length, biases

Figure 8. Comparison of the simulated and observed XCO_2 and XCO_2 enhancements for the OCO-3 across various spatial resolutions (1 km, 2 km, 3 km, 5 km, 10 km, 20 km, 30 km). The first row presents simulated results based on UNAM_EMI and CASA, while the second row displays results based on ODIAC and CASA. The first column illustrates XCO_2 values, the second column showcases ΔXCO_2 values, and the third column provides a histogram depicting simulated and observed values.

decrease by approximately 0.26 ppm for UNAM_EMI (from 0.26 to 0 ppm) and by 0.13 ppm for ODIAC (from −0.08 ppm to −0.21 ppm). These discrepancies arise from two main factors: (a) Differences in the AK and SZA from the FTIR and OCO-3 instruments influence the simulated anthropogenic and biogenic ΔXCO_2 values. (b) Observed ΔXCO_2 variations between OCO-3 and FTIR. Regarding point (a), Figure S3 in Supporting Information S1 illustrates how disparities in AK and SZA influence the simulated anthropogenic ΔXCO_2 values for FTIR and OCO-3, leading to biases of 0.27 (±0.43) ppm for UNAM_EMI and 0.15 (±0.29) ppm for ODIAC. Regarding point (b), the observed ΔXCO_2 variations with CAMS background in FTIR are 0.23 ppm lower than in OCO-3 (as introduced in the first paragraph of Section 3.3). Therefore, the simulated-observed bias for FTIR and OCO-3 should be around 0.5 ppm (0.27 ppm from point a minus −0.23 ppm from point b) in UNAM_EMI, and 0.38 ppm (0.15 ppm minus −0.23 ppm) in ODIAC. Finally, as mentioned earlier, the difference is 0.26 ppm in UNAM_EMI and 0.13 ppm in ODIAC, which is lower than when using only the average bias to calculate (0.5 ppm for UNAM_EMI and 0.38 ppm for ODIAC).

4. Discussion

The ability of OCO-3 SAMs to provide detailed intra-urban observations offers a unique opportunity to enhance our understanding of urban carbon dioxide emissions. However, acknowledging the uncertainty in satellite observation precision, we employed a dense FTIR network over MCMA to validate the accuracy of OCO-3 measurements. Our analysis indicates that OCO-3 XCO_2 levels are higher than those measured by the FTIR network, with a mean bias of 1.06 ± 1.08 ppm. Kiel et al. (2021) discovered that OCO-3 measurements closely align with co-located TCCON observations in Los Angeles, yielding an RMSE of 0.23 ppm. M. Zhou et al. (2022) observed that OCO-3 measurements consistently surpassed ground-based readings in various settings. Specifically, at the COCCON site in Beijing, OCO-3 XCO_2 were 0.64 ppm higher than FTIR measurements, and at the TCCON station in Xianghe, the difference increased to 1.2 ppm. Remarkably, this discrepancy widened during exclusive examinations of SAM observations, escalating to 0.92 ppm in Beijing and 1.48 ppm in Xianghe.

The differences in XCO_2 between two sites are directly proportional to the emissions between those sites (Chen et al., 2016), making the XCO_2 gradients crucial for inferring the sources of emissions. Our analysis revealed that site-to-site differences observed by OCO-3 and FTIR exhibit a bias of approximately 0.3 ppm. Notably, these differences become more pronounced and aligned when focusing exclusively on urban-rural sites, which show a strong correlation ($R = 0.92$), as opposed to intra-urban sites, where the correlation significantly drops ($R = 0.24$). These results closely align with the findings of Rißmann et al. (2022), who documented XCO_2 differences of 0.31 ppm and R of 0.68 for OCO-2 and FTIR measurements in Munich. Additionally, observations from Beijing indicate that the urban-rural differences captured through 5 OCO-3 SAM overpasses correlate strongly with FTIR measurements, showing a mean bias of 0.35 ppm and a correlation coefficient of 0.82 (M. Zhou et al., 2022). These studies consistently show that the site-to-site gradients observed by FTIR are approximately 0.3 ppm lower than those observed by OCO-3. This discrepancy primarily stems from differences in the averaging kernels between FTIR (specifically EM27/SUN in these instances) and OCO-3, with the impact of varying a priori values across instruments being minimal.

The comparison of simulated XCO_2 enhancements with observed values reveals that UNAM_EMI, exhibiting regression slopes closer to 1 than ODIAC, more accurately mirrors the spatial distribution of actual CO_2 emissions. However, the lower bias in ODIAC suggests that its estimates of the total emissions over MCMA may more closely reflect the true emissions. Upon evaluating the simulated values across different sites, it becomes evident that urban sites yield better performance metrics than rural sites (e.g., AMEC, ALTZ). Notably, both AMEC and ALTZ exhibit weak or even negative correlations with the models (R of -0.2 for both UNAM_EMI and ODIAC). This reduced accuracy/quality of the simulations at the AMEC and ALTZ sites is potentially due to low anthropogenic emissions and thus proportionally higher biogenic emissions, which have higher uncertainties associated with them because of the mismatched years in the biogenic emissions data. In the OCO-3 simulation analysis, the initial data at 1 km resolution demonstrated a limited alignment with the observed measurements, evidenced by weak correlation and notable bias. However, substantial enhancements in agreement with observational data were observed upon aggregating the spatial resolution of OCO-3 soundings. By adjusting the resolution to a range of 10–30 km, the results achieved a notable consistency, closely mirroring those derived from FTIR simulations. This indicates that OCO-3 can capture the urban signals, but largely affected by the observation errors. Consolidating the data and reducing the resolution proves effective in minimizing these random errors, thereby ensuring a closer alignment with the FTIR simulation results. This observed uniformity between FTIR and OCO-3 observational and simulation data underscores the reliability of the inventory's performance.

Due to the limited number of observed values at the background site, we constructed boundary values using the 4-D CAMS model. Prior to this, we carefully selected observations from background sites minimally influenced by anthropogenic or biogenic sources to correct CAMS background values. The background measurements from OCO-3 exhibited closer alignment with the CAMS results (0.11 ± 0.25 ppm) compared to those from FTIR (1.34 ± 0.55 ppm). However, this does not allow us to definitively conclude which of CAMS or OCO-3 is more accurate. Our approach aimed to adjust the CAMS background values for OCO-3 and FTIR individually, thus ensuring the urban gradients observed by OCO-3 and FTIR were in alignment. This step is vital for refining emissions calculations and guarantees that the emission estimates remain unaffected by the discrepancies in XCO_2 measurements across different instruments. Subsequently, we utilized the corrected CAMS boundaries values as background, combined them with simulated XCO_2 enhancements from anthropogenic and biogenic

sources for each site. A comparison of statistical metrics (e.g., correlation coefficients, bias, or fitting functions) with those derived solely from observed values revealed similar results. This similarity suggests that corrected CAMS can serve as a viable alternative when complete background observations are unavailable. Such findings underscore the reliability of CAMS background concentrations, reinforcing the model's potential as a substitute in the absence of comprehensive background observations.

Our analysis suggests that the approach of utilizing CAMS corrections as a background can be effectively applied to other studies, particularly those involving FTIR. Given that FTIR operates exclusively under cloudless conditions, obtaining simultaneous observed values from urban areas and their backgrounds is challenging. Thus, employing corrected CAMS enhances the efficiency and maximizes the utility of observations. In the Lagrangian inversion methodology, it is crucial that the enhancements observed in urban areas relative to the background serve as the primary factor for refining the final outcomes. Without adjusting the background, the input urban enhancements may appear anomalous and misaligned with actual observations. Our study highlights the promising potential of integrating OCO-3 and FTIR data for urban CO_2 emissions studies.

5. Conclusion

The MCMA is a densely populated region, confined within a large basin where the emitted anthropogenic CO_2 molecules are easily trapped under low wind conditions due to the steep terrain. Our study demonstrates the potential use of FTIR and OCO-3 SAMs observations to characterize intra-urban and urban-to-rural gradients from the MCMA. The locations of each FTIR site were selected mainly based on the current inventories, which are classified as urban (UNAM, VALL, BOXO), suburban (CUAT, TECA) and background sites (AMEC, ALTZ). Observations in urban sites are usually higher than background sites by 0.36 ~1.38 ppm on average. We matched the observed XCO_2 from FTIRs and OCO-3, both spatially and temporally, with a positive bias of 1.06 ± 1.08 ppm in OCO-3 retrievals compared to FTIR data. XCO_2 concentrations from our FTIR background site (AMEC) show a larger bias compared to the rest of the network (1.35 ± 1.35 ppm). OCO-3 was in better agreement with FTIR when considering urban-to-rural gradients (R of 0.92, mean bias of 0.3ppm) compared to intra-urban gradients (R of 0.24, mean bias of 0.31ppm). When analyzing the absolute XCO_2 concentrations, both background sites (AMEC and ALTZ) were insufficient to provide a continuous data set (clouds, aerosols,…) able to characterize the urban gradients over the entire observation period. To address this, we reconstructed the background concentrations by extracting slant background columns from CAMS 4D fields (depending on the AK and a priori profiles) at the trajectory endpoints, enabling us to enhance our urban gradient analysis. The comparison of modeled and observed background values shows high correlation values (R of 0.97 for FTIR, R of 1.0 for OCO-3) but with a systematic error affecting the entire network (mean bias of 1.34 ppm for FTIR, 0.11 ppm for OCO-3). A bias correction was applied to calibrate our network before examining the XCO_2 gradients.

The simulated XCO_2 using X-STILT footprints shows a high correlation with observations (R of ~0.9) but the simulations of urban enhancements (ΔXCO_2) are more challenging to simulate (R of ~0.6) for both FTIR and OCO-3. For FTIR sensors, the correlation and regression slopes of the simulated CAMS-based urban-rural gradients (R of 0.53 ~0.58, slopes of 0.69 ~0.99 ppm ppm^{-1}) are close to the urban gradients without involving any CAMS background (R of 0.53 ~0.57, slopes of 0.66 ~0.99 ppm ppm^{-1}), indicating the good performance of our background calculation method. Simulated ΔXCO_2 at urban sites were more comparable to the observed values than background sites for FTIR, mostly due to larger biogenic signatures impacting background stations. For OCO-3, our simulations showed a better agreement with observations when aggregating them at coarser resolutions, suggesting that measurement noise plays an important role in OCO-3 SAM's. After aggregating, both correlation coefficients and regression slopes are similar to FTIR's urban sites. Finally, we examined the mean errors in our simulations and in the observations, with noticeable differences in FTIR (−0.12 ~0.18 ppm) and OCO-3 concentrations (0.13 ~0.22 ppm). But these biases remain low, mostly caused by differences in the Averaging Kernels and the a priori profile differences from these two instruments. Correlation coefficients calculated from UNAM_EMI (R of 0.61) are larger than ODIAC (R of 0.52) and the regression slope based on UNAM_EMI (slope of 0.88 ppm ppm^{-1}) are closer to 1:1 line than ODIAC (slope of 0.65 ppm ppm^{-1}), either in overall situation or single site, indicating the distribution of CO_2 emissions in UNAM_EMI might be in better agreement with actual emissions.

Urban gradients across XCO_2 measurement sites have been assimilated in previous inversion studies to produce city-scale emissions. But combining diverse data streams (e.g., from FTIR and OCO-3) might enable us to better

identify intra-urban gradients and to quantify urban CO_2 emissions at high resolution. XCO_2 values from OCO-3 were found to be positively biased compared to FTIR's, but their urban gradients remain similar in magnitude, once corrected for instrument specificities. XCO_2 simulations required column footprints generated by X-STILT and trajectory-based column background values from the CAMS global model. However, modeled background values from coarser global models still contain large uncertainties. A simple bias correction method was used in this study but the real background correction varies with time and location (Jones et al., 2021). Therefore, a Lagrangian inversion framework with state vectors involving background values is essential to refine the background corrections, and to potentially improve current inventories at fine scales (district level or gridded across the MCMA).

Data Availability Statement

The FTIR observation data are accessible on (Ramonet et al., 2024). The OCO-3 Level 2 bias-corrected XCO_2 data (version 10.4r) are available for download from (OCO-2/OCO-3 Science Team et al., 2022). The ERA5 data are accessible at (Hersbach et al., 2022). CAMS global inversion-optimized greenhouse gas concentrations are accessible at the Copernicus Climate Change Service (C3S) Climate Data Store (CDS) (Chevallier, 2013; Chevallier et al., 2019, 2023). The ODIAC emission inventory is documented in Oda and Maksyutov (2015). The source code for the WRF version 3.9.1.1 model (freely available) are available https://www2.mmm.ucar.edu/wrf. Additionally, the source code for the UNAM_EMI model employed in this research (freely available) is detailed in García-Reynoso et al. (2018), and the source code for the X-STILT model used in this study (freely available) can be found in Wu et al. (2019). All figures were produced using the matplotlib package version 3.3.4 in Python 3.7, as introduced by Hunter (2007).

References

Alberti, C., Hase, F., Frey, M., Dubravica, D., Blumenstock, T., Dehn, A., et al. (2022). Improved calibration procedures for the EM27/SUN spectrometers of the COllaborative Carbon Column Observing Network (COCCON). *Atmospheric Measurement Techniques*, *15*(8), 2433–2463. https://doi.org/10.5194/amt-15-2433-2022

Baylon, J. L., Stremme, W., Grutter, M., Hase, F., & Blumenstock, T. (2017). Background CO_2 levels and error analysis from ground-based solar absorption IR measurements in central Mexico. *Atmospheric Measurement Techniques*, *10*(7), 2425–2434. https://doi.org/10.5194/amt-10-2425-2017

Belikov, D. A., Maksyutov, S., Ganshin, A., Zhuravlev, R., Deutscher, N. M., Wunch, D., et al. (2017). Study of the footprints of short-term variation in XCO_2 observed by TCCON sites using NIES and FLEXPART atmospheric transport models. *Atmospheric Chemistry and Physics*, *17*(1), 143–157. https://doi.org/10.5194/acp-17-143-2017

Borsdorff, T., García Reynoso, A., Maldonado, G., Mar-Morales, B., Stremme, W., Grutter, M., & Landgraf, J. (2020). Monitoring CO emissions of the metropolis Mexico City using TROPOMI CO observations. *Atmospheric Chemistry and Physics*, *20*(24), 15761–15774. https://doi.org/10.5194/acp-20-15761-2020

Butz, A., Hanft, V., Kleinschek, R., Frey, M. M., Müller, A., Knapp, M., et al. (2022). Versatile and targeted validation of space-borne XCO_2, XCH_4 and XCO observations by mobile ground-based direct-sun spectrometers. *Frontiers in Remote Sensing*, *2*, 775805. https://doi.org/10.3389/frsen.2021.775805

Cai, Z., Che, K., Liu, Y., Yang, D., Liu, C., & Yue, X. (2021). Decreased anthropogenic CO_2 emissions during the COVID-19 pandemic estimated from FTS and MAX-DOAS measurements at urban Beijing. *Remote Sensing*, *13*(3), 517. https://doi.org/10.3390/rs13030517

Che, K., Cai, Z., Liu, Y., Wu, L., Yang, D., Chen, Y., et al. (2022). Lagrangian inversion of anthropogenic CO_2 emissions from Beijing using differential column measurements. *Environmental Research Letters*, *17*(7), 075001. https://doi.org/10.1088/1748-9326/ac7477

Chen, J., Viatte, C., Hedelius, J. K., Jones, T., Franklin, J. E., Parker, H., et al. (2016). Differential column measurements using compact solar-tracking spectrometers. *Atmospheric Chemistry and Physics*, *16*(13), 8479–8498. https://doi.org/10.5194/acp-16-8479-2016

Chen, J., Zhao, F., Zeng, N., & Oda, T. (2020). Comparing a global high-resolution downscaled fossil fuel CO_2 emission dataset to local inventory-based estimates over 14 global cities. *Carbon Balance and Management*, *15*(1), 1–15. https://doi.org/10.1186/s13021-020-00146-3

Chevallier, F. (2013). On the parallelization of atmospheric inversions of CO_2 surface fluxes within a variational framework. *Geoscientific Model Development*, *6*(3), 783–790. https://doi.org/10.5194/gmd-6-783-2013

Chevallier, F., Lloret, Z., Cozic, A., Takache, S., & Remaud, M. (2023). Toward high-resolution global atmospheric inverse modeling using graphics accelerators. *Geophysical Research Letters*, *50*(5), e2022GL102135. https://doi.org/10.1029/2022GL102135

Chevallier, F., Remaud, M., O'Dell, C. W., Baker, D., Peylin, P., & Cozic, A. (2019). Objective evaluation of surface-and satellite-driven carbon dioxide atmospheric inversions. *Atmospheric Chemistry and Physics*, *19*(22), 14233–14251. https://doi.org/10.5194/acp-19-14233-2019

Crisp, D., Atlas, R. M., Breon, F.-M., Brown, L., Burrows, J., Ciais, P., et al. (2004). The orbiting carbon observatory (OCO) mission. *Advances in Space Research*, *34*(4), 700–709. https://doi.org/10.1016/j.asr.2003.08.062

De Mazière, M., Thompson, A. M., Kurylo, M. J., Wild, J. D., Bernhard, G., Blumenstock, T., et al. (2018). The Network for the Detection of Atmospheric Composition Change (NDACC): History, status and perspectives. *Atmospheric Chemistry and Physics*, *18*(7), 4935–4964. https://doi.org/10.5194/acp-18-4935-2018

Deng, A., Lauvaux, T., Davis, K. J., Gaudet, B. J., Miles, N., Richardson, S. J., et al. (2017). Toward reduced transport errors in a high resolution urban CO_2 inversion system. *Elem Sci Anth*, *5*, 20. https://doi.org/10.1525/elementa.133

Dietrich, F., Chen, J., Voggenreiter, B., Aigner, P., Nachtigall, N., & Reger, B. (2021). MUCCnet: Munich urban carbon column network. *Atmospheric Measurement Techniques*, *14*(2), 1111–1126. https://doi.org/10.5194/amt-14-1111-2021

Feng, S., Lauvaux, T., Newman, S., Rao, P., Ahmadov, R., Deng, A., et al. (2016). Los Angeles megacity: A high-resolution land-atmosphere modelling system for urban CO_2 emissions. *Atmospheric Chemistry and Physics*, *16*(14), 9019–9045. https://doi.org/10.5194/acp-16-9019-2016

Feng, S., Lauvaux, T., Williams, C. A., Davis, K. J., Zhou, Y., Baker, I., et al. (2021). Joint CO_2 mole fraction and flux analysis confirms missing processes in CASA terrestrial carbon uptake over North America. *Global Biogeochemical Cycles*, *35*(7), e2020GB006914. https://doi.org/10.1029/2020GB006914

Frey, M., Sha, M. K., Hase, F., Kiel, M., Blumenstock, T., Harig, R., et al. (2019). Building the COllaborative carbon column observing network (COCCON): Long-term stability and ensemble performance of the EM27/SUN fourier transform spectrometer. *Atmospheric Measurement Techniques*, *12*(3), 1513–1530. https://doi.org/10.5194/amt-12-1513-2019

García-Reynoso, J. A., Mar-Morales, B. E., & Ruiz-Suárez, L. G. (2018). Modelo de distribución espacial, temporal y de especiación del inventario de emisiones de méxico (año base 2008) para su uso en modelización de calidad del aire (diete). *Revista Internacional de Contaminación Ambiental*, *34*(4), 635–649. https://doi.org/10.20937/RICA.2018.34.04.07

Gately, C. K., & Hutyra, L. R. (2017). Large uncertainties in urban-scale carbon emissions. *Journal of Geophysical Research: Atmospheres*, *122*(20), 11–242. https://doi.org/10.1002/2017JD027359

Gisi, M., Hase, F., Dohe, S., Blumenstock, T., Simon, A., & Keens, A. (2012). XCO_2-measurements with a tabletop FTS using solar absorption spectroscopy. *Atmospheric Measurement Techniques*, *5*(11), 2969–2980. https://doi.org/10.5194/amt-5-2969-2012

Gurney, K. R., Liang, J., Roest, G., Song, Y., Mueller, K., & Lauvaux, T. (2021). Under-reporting of greenhouse gas emissions in US cities. *Nature Communications*, *12*(1), 553. https://doi.org/10.1038/s41467-020-20871-0

Hase, F., Frey, M., Blumenstock, T., Groß, J., Kiel, M., Kohlhepp, R., et al. (2015). Application of portable FTIR spectrometers for detecting greenhouse gas emissions of the major city Berlin. *Atmospheric Measurement Techniques*, *8*(7), 3059–3068. https://doi.org/10.5194/amt-8-3059-2015

Hase, F., Frey, M., Kiel, M., Blumenstock, T., Harig, R., Keens, A., & Orphal, J. (2016). Addition of a channel for XCO observations to a portable FTIR spectrometer for greenhouse gas measurements. *Atmospheric Measurement Techniques*, *9*(5), 2303–2313. https://doi.org/10.5194/amt-9-2303-2016

Hase, F., Hannigan, J., Coffey, M., Goldman, A., Höpfner, M., Jones, N., et al. (2004). Intercomparison of retrieval codes used for the analysis of high-resolution, ground-based FTIR measurements. *Journal of Quantitative Spectroscopy and Radiative Transfer*, *87*(1), 25–52. https://doi.org/10.1016/j.jqsrt.2003.12.008

Hersbach, H., Bell, B., Berrisford, P., Biavati, G., Horányi, A., Muñoz Sabater, J., et al. (2022). ERA5 hourly data on single levels from 1940 to present [Dataset]. *Copernicus Climate Change Service (C3S) Climate Data Store (CDS)*. https://doi.org/10.24381/cds.adbb2d47

Hsu, A., Höhne, N., Kuramochi, T., Vilariño, V., & Sovacool, B. K. (2020). Beyond states: Harnessing sub-national actors for the deep decarbonisation of cities, regions, and businesses. *Energy Research & Social Science*, *70*, 101738. https://doi.org/10.1016/j.erss.2020.101738

Hu, C., Liu, S., Wang, Y., Zhang, M., Xiao, W., Wang, W., & Xu, J. (2018). Anthropogenic CO_2 emissions from a megacity in the Yangtze River Delta of China. *Environmental Science and Pollution Research*, *25*(23), 23157–23169. https://doi.org/10.1007/s11356-018-2325-3

Hunter, J. D. (2007). Matplotlib: A 2d graphics environment. *Computing in Science & Engineering*, *9*(3), 90–95. https://doi.org/10.1109/MCSE.2007.55

Ionov, D. V., Makarova, M. V., Hase, F., Foka, S. C., Kostsov, V. S., Alberti, C., et al. (2021). The CO_2 integral emission by the megacity of St Petersburg as quantified from ground-based FTIR measurements combined with dispersion modelling. *Atmospheric Chemistry and Physics*, *21*(14), 10939–10963. https://doi.org/10.5194/acp-21-10939-2021

Jones, T. S., Franklin, J. E., Chen, J., Dietrich, F., Hajny, K. D., Paetzold, J. C., et al. (2021). Assessing urban methane emissions using column-observing portable Fourier transform infrared (FTIR) spectrometers and a novel Bayesian inversion framework. *Atmospheric Chemistry and Physics*, *21*(17), 13131–13147. https://doi.org/10.5194/acp-21-13131-2021

Kiel, M., Eldering, A., Roten, D. D., Lin, J. C., Feng, S., Lei, R., et al. (2021). Urban-focused satellite CO_2 observations from the orbiting carbon observatory-3: A first look at the Los Angeles megacity. *Remote Sensing of Environment*, *258*, 112314. https://doi.org/10.1525/elementa.137

Kuhlmann, G., Brunner, D., Broquet, G., & Meijer, Y. (2020). Quantifying CO_2 emissions of a city with the Copernicus Anthropogenic CO_2 Monitoring satellite mission. *Atmospheric Measurement Techniques*, *13*(12), 6733–6754. https://doi.org/10.5194/amt-13-6733-2020

Lauvaux, T., & Davis, K. (2014). Planetary boundary layer errors in mesoscale inversions of column-integrated CO_2 measurements. *Journal of Geophysical Research: Atmospheres*, *119*(2), 490–508. https://doi.org/10.1002/2013JD020175

Lauvaux, T., Gurney, K. R., Miles, N. L., Davis, K. J., Richardson, S. J., Deng, A., et al. (2020). Policy-relevant assessment of urban CO_2 emissions. *Environmental Science & Technology*, *54*(16), 10237–10245. https://doi.org/10.1021/acs.est.0c00343

Lauvaux, T., Miles, N. L., Deng, A., Richardson, S. J., Cambaliza, M. O., Davis, K. J., et al. (2016). High-resolution atmospheric inversion of urban CO_2 emissions during the dormant season of the Indianapolis Flux Experiment (INFLUX). *Journal of Geophysical Research: Atmospheres*, *121*(10), 5213–5236. https://doi.org/10.1002/2015JD024473

Linton, S., Clarke, A., & Tozer, L. (2022). Technical pathways to deep decarbonization in cities: Eight best practice case studies of transformational climate mitigation. *Energy Research & Social Science*, *86*, 102422. https://doi.org/10.1016/j.erss.2021.102422

Maasakkers, J. D., Varon, D. J., Elfarsdóttir, A., McKeever, J., Jervis, D., Mahapatra, G., et al. (2022). Using satellites to uncover large methane emissions from landfills. *Science Advances*, *8*(31), eabn9683. https://doi.org/10.1126/sciadv.abn9683

Messerschmidt, J., Geibel, M., Blumenstock, T., Chen, H., Deutscher, N., Engel, A., et al. (2011). Calibration of TCCON column-averaged CO_2: The first aircraft campaign over European TCCON sites. *Atmospheric Chemistry and Physics*, *11*(21), 10765–10777. https://doi.org/10.5194/acp-11-10765-2011

Molina, L. T., Velasco, E., Retama, A., & Zavala, M. (2019). Experience from integrated air quality management in the Mexico City Metropolitan Area and Singapore. *Atmosphere*, *10*(9), 512. https://doi.org/10.3390/atmos10090512

Monteil, G., & Scholze, M. (2021). Regional CO_2 inversions with LUMIA, the Lund University modular inversion algorithm, v1.0. *Geoscientific Model Development*, *14*(6), 3383–3406. https://doi.org/10.5194/gmd-14-3383-2021

Nassar, R., Napier-Linton, L., Gurney, K. R., Andres, R. J., Oda, T., Vogel, F. R., & Deng, F. (2013). Improving the temporal and spatial distribution of CO_2 emissions from global fossil fuel emission data sets. *Journal of Geophysical Research: Atmospheres*, *118*(2), 917–933. https://doi.org/10.1029/2012JD018196

Nguyen, H., Osterman, G., Wunch, D., O'Dell, C., Mandrake, L., Wennberg, P., et al. (2014). A method for colocating satellite XCO_2 data to ground-based data and its application to ACOS-GOSAT and TCCON. *Atmospheric Measurement Techniques*, *7*(8), 2631–2644. https://doi.org/10.5194/amt-7-2631-2014

OCO-2/OCO-3 Science Team, Chatterjee, A., & Payne, V. (2022). OCO-3 Level 2 bias-corrected XCO_2 and other select fields from the full-physics retrieval aggregated as daily files, Retrospective processing v10.4r [dataset]. Goddard Earth Sciences Data and Information Services Center (GES DISC). https://doi.org/10.5067/970BCC4DHH24

Oda, T., & Maksyutov, S. (2015). ODIAC fossil fuel CO_2 emissions dataset (ODIAC2020) [Dataset]. *Center for Global Environmental Research, National Institute for Environmental Studies.* https://doi.org/10.17595/20170411.001

Oda, T., Maksyutov, S., & Andres, R. J. (2018). The open-source data inventory for anthropogenic CO_2, version 2016 (ODIAC2016): A global monthly fossil fuel CO_2 gridded emissions data product for tracer transport simulations and surface flux inversions. *Earth System Science Data*, *10*(1), 87–107. https://doi.org/10.5194/essd-10-87-2018

O'dell, C. W., Eldering, A., Wennberg, P. O., Crisp, D., Gunson, M. R., Fisher, B., et al. (2018). Improved retrievals of carbon dioxide from orbiting carbon observatory-2 with the version 8 acos algorithm. *Atmospheric Measurement Techniques*, *11*(12), 6539–6576. https://doi.org/10.5194/amt-11-6539-2018

Osterman, G., O'Dell, C., Eldering, A., Fisher, B., Crisp, D., Cheng, C., et al. (2020). Orbiting carbon observatory-2 & 3 data product user's guide Tech. Rep.). v10, Tech. rep., Jet Propulsion Laboratory. Retrieved from https://docserver.gesdisc.eosdis.nasa.gov/public/project/OCO/OCO2_OCO3_B10_DUG.pdf

Pacheco, G., Garcia-Reynoso, A., Stremme, W., Ruiz Suárez, L. G., Clerbaux, C., & Coheur, P.-F. (2020). Carbon monoxide emissions assessment by using satellite and modeling data: Central Mexico case study. *Atmósfera, ER*. https://doi.org/10.20937/ATM.52696

Pérez-Landa, G., Ciais, P., Sanz, M., Gioli, B., Miglietta, F., Palau, J., et al. (2007). Mesoscale circulations over complex terrain in the Valencia coastal region, Spain-Part 1: Simulation of diurnal circulation regimes. *Atmospheric Chemistry and Physics*, *7*(7), 1835–1849. https://doi.org/10.5194/acp-7-1835-2007

Ramonet, M., Grutter, M., Taquet, N., Lopez, M., & Stremme, W. (2024). CO_2 total columns in Mexico-City [Dataset]. https://doi.org/10.57932/4c264750-4eb4-4cf8-9432-1c79048116d3

Rastogi, B., Miller, J. B., Trudeau, M., Andrews, A. E., Hu, L., Mountain, M., et al. (2021). Evaluating consistency between total column CO_2 retrievals from OCO-2 and the in situ network over North America: Implications for carbon flux estimation. *Atmospheric Chemistry and Physics*, *21*(18), 14385–14401. https://doi.org/10.5194/acp-21-14385-2021

Rißmann, M., Chen, J., Osterman, G., Zhao, X., Dietrich, F., Makowski, M., et al. (2022). Comparison of OCO-2 target observations to MUCCnet-is it possible to capture urban XCO_2 gradients from space? *Atmospheric Measurement Techniques*, *15*(22), 6605–6623. https://doi.org/10.5194/amt-15-6605-2022

Rodgers, C. D., & Connor, B. J. (2003). Intercomparison of remote sounding instruments. *Journal of Geophysical Research*, *108*(D3). https://doi.org/10.1029/2002JD002299

Rodríguez Zas, J., & Garcia-Reynoso, A. (2021). ActualizaciÓn del inventario nacional de emisiones de 2013 para la modelaciÓn de la calidad del aire en el centro de mÉxico. *Revista Internacional de Contaminación Ambiental*, *37*, 463–487. https://doi.org/10.20937/RICA.53865

Roten, D., Lin, J. C., Kunik, L., Mallia, D., Wu, D., Oda, T., & Kort, E. A. (2022). The information content of dense carbon dioxide measurements from space: A high-resolution inversion approach with synthetic data from the OCO-3 instrument. *Atmospheric Chemistry and Physics Discussions*, 1–43. https://doi.org/10.5194/acp-2022-315

Sargent, M., Barrera, Y., Nehrkorn, T., Hutyra, L. R., Gately, C. K., Jones, T., et al. (2018). Anthropogenic and biogenic CO_2 fluxes in the Boston urban region. *Proceedings of the National Academy of Sciences*, *115*(29), 7491–7496. https://doi.org/10.1073/pnas.1803715115

Schuh, A. E., Otte, M., Lauvaux, T., & Oda, T. (2021). Far-field biogenic and anthropogenic emissions as a dominant source of variability in local urban carbon budgets: A global high-resolution model study with implications for satellite remote sensing. *Remote Sensing of Environment*, *262*, 112473. https://doi.org/10.1016/j.rse.2021.112473

SEDEMA. (2018). *Sedema secretaría del medio ambiente de la ciudad de méxico: Inventario de emisiones de la ciudad de méxico 2016*. Ciudad de México.

Shekhar, A., Chen, J., Paetzold, J. C., Dietrich, F., Zhao, X., Bhattacharjee, S., et al. (2020). Anthropogenic CO_2 emissions assessment of Nile Delta using XCO_2 and SIF data from OCO-2 satellite. *Environmental Research Letters*, *15*(9), 095010. https://doi.org/10.1088/1748-9326/ab9cfe

Shim, C., Han, J., Henze, D. K., & Yoon, T. (2019). Identifying local anthropogenic CO_2 emissions with satellite retrievals: A case study in South Korea. *International Journal of Remote Sensing*, *40*(3), 1011–1029. https://doi.org/10.1080/01431161.2018.1523585

Sosa, E. R., Vega, E., Wellens, A., Jaimes, M., Fuentes, G. G., Granados, H. E., et al. (2020). Reduction of atmospheric emissions due to switching from fuel oil to natural gas at a power plant in a critical area in Central Mexico. *Journal of the Air & Waste Management Association*, *70*(10), 1043–1059. https://doi.org/10.1080/10962247.2020.1808113

Stocker, T. (2014). *Climate change 2013: The physical science basis: Working group i contribution to the fifth assessment report of the intergovernmental panel on climate change*. Cambridge University Press.

Stremme, W., Grutter, M., Rivera, C., Bezanilla, A., Garcia, A., Ortega, I., et al. (2013). Top-down estimation of carbon monoxide emissions from the Mexico Megacity based on FTIR measurements from ground and space. *Atmospheric Chemistry and Physics*, *13*(3), 1357–1376. https://doi.org/10.5194/acp-13-1357-2013

Taquet, N., Stremme, W., Gonzalez del Castillo, M. E., Almanza, V., Bezanilla, A., Laurent, O., et al. (2024). CO_2 and CO temporal variability over Mexico City from ground-based total column and surface measurements. *EGUsphere*, *2024*, 1–34. https://doi.org/10.5194/egusphere-2024-512

Taylor, T. E., Eldering, A., Merrelli, A., Kiel, M., Somkuti, P., Cheng, C., et al. (2020). OCO-3 early mission operations and initial (vEarly) XCO_2 and SIF retrievals. *Remote Sensing of Environment*, *251*, 112032. https://doi.org/10.1016/j.rse.2020.112032

Tu, Q., Hase, F., Blumenstock, T., Kivi, R., Heikkinen, P., Sha, M. K., et al. (2020). Intercomparison of atmospheric CO_2 and CH_4 abundances on regional scales in boreal areas using Copernicus Atmosphere Monitoring Service (CAMS) analysis, COllaborative Carbon Column Observing Network (COCCON) spectrometers, and Sentinel-5 Precursor satellite observations. *Atmospheric Measurement Techniques*, *13*(9), 4751–4771. https://doi.org/10.5194/amt-13-4751-2020

Vogel, F. R., Frey, M., Staufer, J., Hase, F., Broquet, G., Xueref-Remy, I., et al. (2019). XCO_2 in an emission hot-spot region: The COCCON Paris campaign 2015. *Atmospheric Chemistry and Physics*, *19*(5), 3271–3285. https://doi.org/10.5194/acp-19-3271-2019

Wei, C., Wang, M., Fu, Q., Dai, C., Huang, R., & Bao, Q. (2020). Temporal characteristics of greenhouse gases (CO_2 and CH_4) in the megacity Shanghai, China: Association with air pollutants and meteorological conditions. *Atmospheric Research*, *235*, 104759. https://doi.org/10.1016/j.atmosres.2019.104759

Wu, D., Fasoli, B., & Lin, J. C. (2019). uataq/X-STILT: X-STILT (v1.4.1). [Software]. *Zenodo*. https://doi.org/10.5281/zenodo.2556989

Wu, D., Lin, J. C., Fasoli, B., Oda, T., Ye, X., Lauvaux, T., et al. (2018). A Lagrangian approach towards extracting signals of urban CO_2 emissions from satellite observations of atmospheric column CO_2 (XCO_2): X-stochastic time-inverted Lagrangian transport model ("X-STILT v1"). *Geoscientific Model Development*, *11*(12), 4843–4871. https://doi.org/10.5194/gmd-11-4843-2018

Wunch, D., Toon, G. C., Blavier, J.-F. L., Washenfelder, R. A., Notholt, J., Connor, B. J., et al. (2011). The total carbon column observing network. *Philosophical Transactions of the Royal Society A: Mathematical, Physical & Engineering Sciences*, *369*(1943), 2087–2112. https://doi.org/10.1098/rsta.2010.0240

Xu, Y. (2023). *Analysis of atmospheric CO$_2$ measurements in Mexico City*. Theses, Université Paris-Saclay. Retrieved from https://theses.hal. science/tel-04102800

Yang, D., Boesch, H., Liu, Y., Somkuti, P., Cai, Z., Chen, X., et al. (2020). Toward high precision XCO$_2$ retrievals from TanSat observations: Retrieval improvement and validation against TCCON measurements. *Journal of Geophysical Research: Atmospheres*, *125*(22), e2020JD032794. https://doi.org/10.1029/2020JD032794

Yang, D., Hakkarainen, J., Liu, Y., Ialongo, I., Cai, Z., & Tamminen, J. (2023). Detection of anthropogenic CO$_2$ emission signatures with TanSat CO$_2$ and with Copernicus Sentinel-5 Precursor (S5P) NO$_2$ measurements: First results. *Advances in Atmospheric Sciences*, *40*(40), 1–5. https://doi.org/10.1007/s00376-022-2237-5

Ye, X., Lauvaux, T., Kort, E. A., Oda, T., Feng, S., Lin, J. C., et al. (2020). Constraining fossil fuel CO$_2$ emissions from urban area using OCO-2 observations of total column CO$_2$. *Journal of Geophysical Research: Atmospheres*, *125*(8), e2019JD030528. https://doi.org/10.1029/2019JD030528

Yoshida, Y., Kikuchi, N., Morino, I., Uchino, O., Oshchepkov, S., Bril, A., et al. (2013). Improvement of the retrieval algorithm for GOSAT SWIR XCO$_2$ and XCH$_4$ and their validation using TCCON data. *Atmospheric Measurement Techniques*, *6*(6), 1533–1547. https://doi.org/10.5194/amt-6-1533-2013

Zhao, X., Chen, J., Marschall, J., Gałkowski, M., Hachinger, S., Dietrich, F., et al. (2022). Understanding greenhouse gas (GHG) column concentrations in Munich using WRF. *Atmospheric Chemistry and Physics Discussions*, 1–30. https://doi.org/10.5194/acp-2022-281

Zhao, X., Marshall, J., Hachinger, S., Gerbig, C., Frey, M., Hase, F., & Chen, J. (2019). Analysis of total column CO$_2$ and CH$_4$ measurements in Berlin with WRF-GHG. *Atmospheric Chemistry and Physics*, *19*(17), 11279–11302. https://doi.org/10.5194/acp-19-11279-2019

Zhou, M., Ni, Q., Cai, Z., Langerock, B., Nan, W., Yang, Y., et al. (2022). CO$_2$ in Beijing and Xianghe observed by ground-based FTIR column measurements and validation to OCO-2/3 satellite observations. *Remote Sensing*, *14*(15), 3769. https://doi.org/10.3390/rs14153769

Zhou, Y., Williams, C. A., Lauvaux, T., Davis, K. J., Feng, S., Baker, I., et al. (2020). A multiyear gridded data ensemble of surface biogenic carbon fluxes for North America: Evaluation and analysis of results. *Journal of Geophysical Research: Biogeosciences*, *125*(2), e2019JG005314. https://doi.org/10.1029/2019JG005314